

THE PENNSYLVANIA STATE UNIVERSITY
SCHREYER HONORS COLLEGE

DEPARTMENT OF AEROSPACE ENGINEERING

SHAPE CONTROL OF TENDON-ACTUATED TENSEGRITY STRUCTURES

NATHANIEL S. OSIKOWICZ
SUMMER 2021

A thesis
submitted in partial fulfillment
of the requirements
for a baccalaureate degree
in Aerospace Engineering
with honors in Aerospace Engineering

Reviewed and approved* by the following:

Puneet Singla
Professor of Aerospace Engineering
Thesis Supervisor

Robert Melton
Professor of Aerospace Engineering
Honors Advisor

*Electronic approvals are on file.

Abstract

As we further extend our reach into outer space, there exists an unmet need for autonomous agents to carry out highly dexterous manipulation tasks such as on-orbit servicing and habitat construction. In order to be packaged efficiently for transport and autonomously deployed at a remote destination, these robotic mechanisms must be lightweight, yet highly articulated. Tensegrity structures, which comprise a continuous tendon network, are a suitable candidate for carrying out dexterous manipulation tasks in outer space. This thesis focuses on controlling the shape of tensegrity structures by changing the tension in the supporting tendons.

A vector-based approach is used to model the multi-body dynamics of tensegrity structures in a non-minimal coordinate system. By modeling the dynamics of each bar member with 6 degrees of freedom rather than 5, we avoid the use of transcendental functions to improve the accuracy of numerical simulations. This methodology is further extended to handle Class-k structures by modeling bar contact forces as Lagrange constraint forces. A reduced-order model is then constructed to solve for the corresponding Lagrange multipliers in closed-form. Leveraging the vector-based dynamics model, a state feedback controller is developed to regulate the shape of a tensegrity structure to a desired reference trajectory. We define the control variable as the string force density to make the governing equations of motion linear in the control variable. This allows the required string force density to be solved for linearly at each time step by solving a convex linear programming problem. The developed control law is implemented in simulation on several Class-1 and Class-k tensegrity structures, clearly showing the effectiveness of the developed ideas in modeling and control of tensegrity structures. Combining our results, we develop a novel robotic manipulator by using self-similar iterations to yield a structure that is both highly dexterous and lightweight, proving that the modeling and control framework can be used to design complex engineering structures.

Table of Contents

List of Figures	v
List of Symbols	vii
Acknowledgments	x
Chapter 1	
Introduction	1
1.1 Historical Background	2
1.2 Objectives	4
1.3 Definitions	4
1.4 Overview	6
Chapter 2	
Tensegrity System Dynamics	8
2.1 Vector Notation	8
2.2 Vector Kinematics	9
2.3 Dynamics of a Single Bar	11
2.3.1 Rotational Dynamics	11
2.3.2 Translational Dynamics	15
2.4 Matrix Formulation of Tensegrity Dynamics	15
2.5 Class-k Tensegrity Systems	19
2.6 Reduced-order Dynamics	20
2.7 Dynamics Verification: Double Pendulum	22
2.7.1 Analytical Solution	23
2.7.2 Numerical Solution	24
2.8 Class-1 Dynamics Verification: T-bar Simulation	26
2.9 Class-k Dynamics Verification: D-bar Simulation	29
Chapter 3	
Model-based Shape Control	32
3.1 State Feedback	33
3.2 Shape Objectives	34
3.3 Stability Considerations	34

3.4	Position Control	35
3.5	Velocity and Acceleration Control	37
3.6	Control Law Implementation	39
3.7	Case Study: T-bar Position Control	40
3.8	Case Study: D-bar Position Control	43
Chapter 4		
	Tensegrity Robotic Arm	47
4.1	Self-Similar Iterations	47
4.2	Three-Dimensional Systems	49
4.3	T_2D_1 Robotic Arm Extension	50
Chapter 5		
	Conclusions and Future Work	55
5.1	Conclusions	55
5.2	Future Work	58
5.2.1	Experimental Verification	58
5.2.2	Optimal and Robust Control Strategies	60
Appendix A		
	Elastic String Modeling	61
Appendix B		
	Tensegrity Dynamics Flow Charts	62
Appendix C		
	Analytical Solution for the Class-K Lagrange Multiplier	64

List of Figures

1.1	Deployment of a fractal-based tensegrity robotic arm	1
1.2	Tensegrity in art and nature	2
1.3	NASA Super Ball Bot [26]	3
1.4	Tensegrity definition	4
1.5	Tensegrity classification	5
2.1	Direction cosines	9
2.2	A single bar member	11
2.3	Numbering convention of a single bar	15
2.4	Double pendulum system	23
2.5	Comparison between double pendulum analytical and numerical solution	25
2.6	T-bar tensegrity system with different initial conditions	26
2.7	Initial condition response of the horizontally preloaded T-bar system . .	28
2.8	D-bar tensegrity system with different initial conditions	30
2.9	Initial condition response of the vertically preloaded D-bar system	31
3.1	Quasi-static shape change	33
3.2	T-bar position control sequence	41

3.3	T-bar position control simulation results	42
3.4	Modified D-bar structure	43
3.5	D-bar position control sequence	45
3.6	D-bar position control simulation results	46
4.1	T-bar self-similar iterations	48
4.2	Two-dimensional T_2D_1 configuration	48
4.3	Basic three-dimensional structures	49
4.4	T_2D_1 fractal-based robotic arm deployment	51
4.5	Desired node trajectories	52
4.6	T_2D_1 robotic arm position control sequence	53
4.7	T_2D_1 robotic arm extension simulation results	54
5.1	Hardware implementation of the cylindrical triplex	58
5.2	Visual feedback of the cylindrical triplex	59
B.1	Class-1 dynamics flow chart	62
B.2	Class-k dynamics flow chart	63

List of Symbols

- α Total number of strings in a tensegrity structure, p. 15
- \mathbf{b} Bar vector, p. 11
- β Total number of bars in a tensegrity structure, p. 15
- B Bar matrix, p. 16
- \mathcal{B} Body Reference Frame Vectrix, p. 10
- c Total number of constraints in a Class-k tensegrity structure, p. 20
- C_b Bar connectivity matrix, p. 16
- C_r Bar center of mass connectivity matrix, p. 16
- C_s String connectivity matrix, p. 16
- $\mathcal{C}^{\mathcal{BN}}$ DCM which maps the inertial frame to the body-fixed frame, p. 19
- D Class-k constraint matrix, right, p. 20
- E_p Position control error matrix p. 37
- E_v Velocity control error matrix p. 38
- E_a Acceleration control error matrix p. 38
- \mathbf{f}_i Arbitrary force vector acting acting on node n_i , p. 13
- F Total force matrix, p. 17
- η_1 Reduced order Class-K no-motion space basis vectors, p. 21
- η_2 Reduced order Class-K constrained node coordinates, p. 21
- γ String force density vector, p. 19
- h Number of controller “nodes of interest”, p. 34

- \mathbf{h} Bar angular momentum vector, p. 12
- I_b Bar moment of inertia, p. 12
- j Number of controller “axes of interest”, p. 34
- J Modified bar moment of inertia, p. 13
- k String extensional stiffness, p. 61
- K ‘Stiffness’ matrix in EOMs, p. 19
- l Bar length, p. 11
- L_p Control objective matrix for axis selection (position control case), p. 37
- L_v Control objective matrix for axis selection (velocity control case), p. 38
- L_a Control objective matrix for axis selection (acceleration control case), p. 38
- \mathcal{L} Lagrangian, p. 24
- $\boldsymbol{\lambda}$ Bar force density vector, p. 17
- m_b Bar mass, p. 13
- \mathbf{m} Bar mass vector, p. 17
- M ‘Mass’ matrix in EOMs, p. 19
- n Total number of nodes in a tensegrity structure, p. 16
- \mathbf{n} Node vector, p. 16
- N Node matrix, p. 16
- \mathcal{N} Inertial (Global) Reference Frame Vectrix, p. 10
- n Total number of nodes in a tensegrity structure, p. 16
- $\boldsymbol{\omega}_b$ Bar angular velocity vector, p. 12
- Ω Lagrange multiplier matrix, p. 20
- P Class-k constraint matrix, left, p. 20
- Ψ Derivative gain matrix, p. 35
- ρ String rest length, p. 61
- r_b Bar radius, p. 13

- \mathbf{r} Bar center of mass vector, p. 11
- R Bar center of mass matrix, p. 16
- R_p Control objective matrix for node position selection, p. 37
- R_v Control objective matrix for node velocity selection, p. 38
- R_a Control objective matrix for node acceleration selection, p. 38
- \mathbf{s} String vector, p. 16
- S String matrix, p. 16
- Σ Class-k constraint singular values, p. 21
- \mathbf{t} String tension vector, p. 18
- T String tension matrix, p. 18
- $\boldsymbol{\tau}$ Sum of torques acting about a bar's center of mass, p. 13
- Θ Proportional gain matrix, p. 34
- U Class-k constraint left-singular vectors, p. 21
- V Class-k constraint right-singular vectors, p. 21
- \mathbf{w}_i External force vector acting acting on node n_i , p. 18
- W External force matrix, p. 18
- \bar{Y}_p Shape trajectory matrix, p. 37
- \bar{Y}_v Velocity trajectory matrix, p. 38
- \bar{Y}_a Acceleration trajectory matrix, p. 38
- z String damping constant, p. 61

Acknowledgments

I would like to thank my research advisor, Dr. Puneet Singla, for his endless support and mentorship throughout the course of my academic journey. His many teachings have provided an environment in which I could be challenged and enlightened academically. I am very thankful to have been introduced to dynamics and control through Dr. Singla. His lectures have always inspired me to look beyond the face value of an equation.

I'd also like to thank my academic advisors, Dr. Melton and Dr. Lesieutre, as well as department head, Dr. Pritchett, in the aerospace engineering department. Dr. Melton has supported me since the very beginning of my studies, helping me progress academically in ways that I couldn't have imagined. Dr. Lesieutre has played a crucial role in my discovery of academic research, which I am very thankful for. It was a pleasure to be a student in the aerospace department with Dr. Pritchett as the department head. She always went out of her way to make students feel acknowledged and appreciated. I would also like to thank Erin Hostetler, whose guidance and encouragement in the REU program greatly enriched my thesis research.

Finally, to my family and friends, thanks for always being there to cheer me up. I couldn't go without mentioning members of the AIAA executive board, Kellie, Nick, and Taelor, who kept the aerospace spirit alive during our weekly meetings. Also, thanks to Himavath Jois for his friendship and mentorship through the IUG program. The importance of a good mentor cannot be overstated. Lastly, to my rock climbing partners, Quin, Kevi, and Nelson, thanks for helping me to not take life too seriously and for double checking my knots when the thesis was the only thing on my mind.

This material is based upon work supported by the NASA Pennsylvania Space Grant Consortium and the U.S. Government. Any opinions, findings, and conclusions or recommendations expressed in this material are those of the author and do not necessarily reflect the views of the NASA Pennsylvania Space Grant Consortium.

Chapter 1 | Introduction

With NASA's lunar exploration missions slated for the end of the decade and plans to send the first astronauts to Mars right around the corner, humankind marches towards its next giant leap in outer space. Our return to the lunar surface will rely upon seamless and efficient operation in cislunar space, the volume between Earth and the moon. To provide vital life support for the lunar astronauts and facilitate the transport of rovers and other robots, NASA is currently developing the Lunar Gateway, a moon-orbiting outpost [1, 2]. Still, plans of establishing a lunar gateway and colonizing the red planet are faced with the difficult challenge of constructing large-scale habitats in the low-gravity environment of outer space. At that, the payload costs associated with NASA's Journey to Mars remain a significant financial hurdle, making it difficult for policy makers to fund such an ambitious plan. To this end, there is an unmet need for lightweight space robots with autonomous construction capabilities.

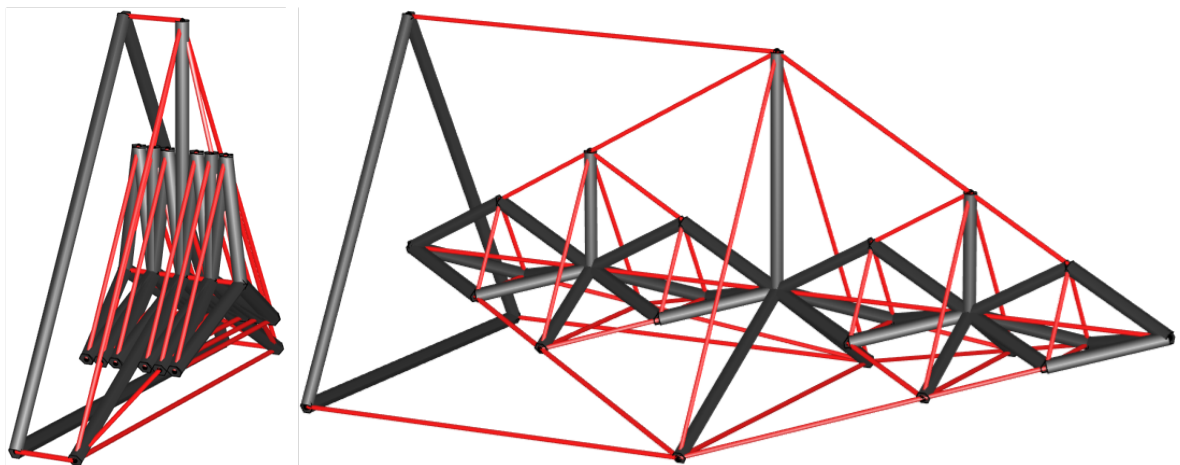


Figure 1.1. Deployment of a fractal-based tensegrity robotic arm

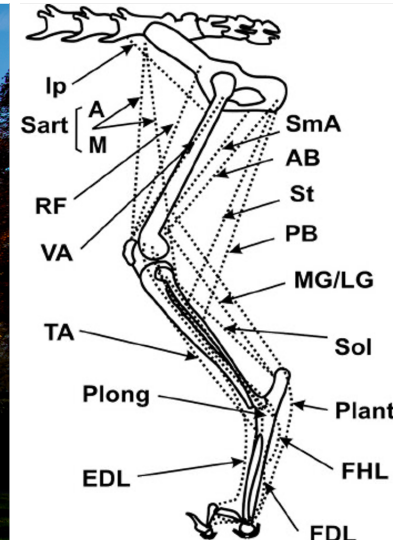
Recent results suggest that the tensegrity structure, an example of which is depicted in Figure 1.1, is a minimal mass structure subject to a stiffness constraint [3]. In this research, we aim to exploit this realization by developing a model-based tensegrity shape control law with a specific focus on dexterous manipulation.

1.1 Historical Background

Buckminster Fuller first coined the word *tensegrity* in the 1950s as a conjunction of the two words *tension* and *integrity* [3,4]. Though the exact origin of tensegrity is debated, the first physical tensegrity was built by American sculptor Kenneth Snelson as an art installation [5]. One such example of Snelson’s work can be found outside the Hirshhorn Museum and Sculpture Garden in Washington D.C. ‘Needle Tower’ (Figure 1.2(a)), as it is named, showcases the visual elegance of tensegrity structures. Due to its presence in membranes and tissues [6–8], as well as in mammalian musculoskeletal systems [9,10], tensegrity has been referred to as ‘The Architecture of Life’ [11]. Figure 1.2(b) shows the flexor and extensor tendons in a cat’s hind legs, which can be idealized by tensegrity. Its artistic beauty, presence in nature, minimal-mass characteristics and shape morphability have turned tensegrity research into an interesting point of convergence for artists, biologists, and engineers alike.



(a) Needle Tower tensegrity sculpture [12]



(b) Cat hind leg [13]

Figure 1.2. Tensegrity in art and nature

To date, the majority of tensegrity research has been centered around applications for deployable and compliant structures [14–16]. Thus, many advancements have been made in tensegrity statics [17] and kinematic analysis [18]. In recent decades, interest in tensegrity has shifted from static analysis to dynamic analysis. As a result, a handful of dynamic models have been developed for different tensegrity systems [19–21] leading to advancements in the actuation and control of tensegrity structures [22–24]. One notable result is the Super Ball Bot developed at NASA Ames (Figure 1.3) which uses evolutionary algorithms to change its center of mass by altering cable lengths, resulting in a rolling motion [25,26]. Other bio-inspired tensegrity structures have emerged mimicking fish [27], joints [28], hands [29], and feet [30]. Despite these recent advancements in the dynamics and control of tensegrity systems, current tensegrity modeling and simulation packages focus on very particular topologies. There is still a need to develop a unifying control framework facilitating the shape change of any given tensegrity structure.

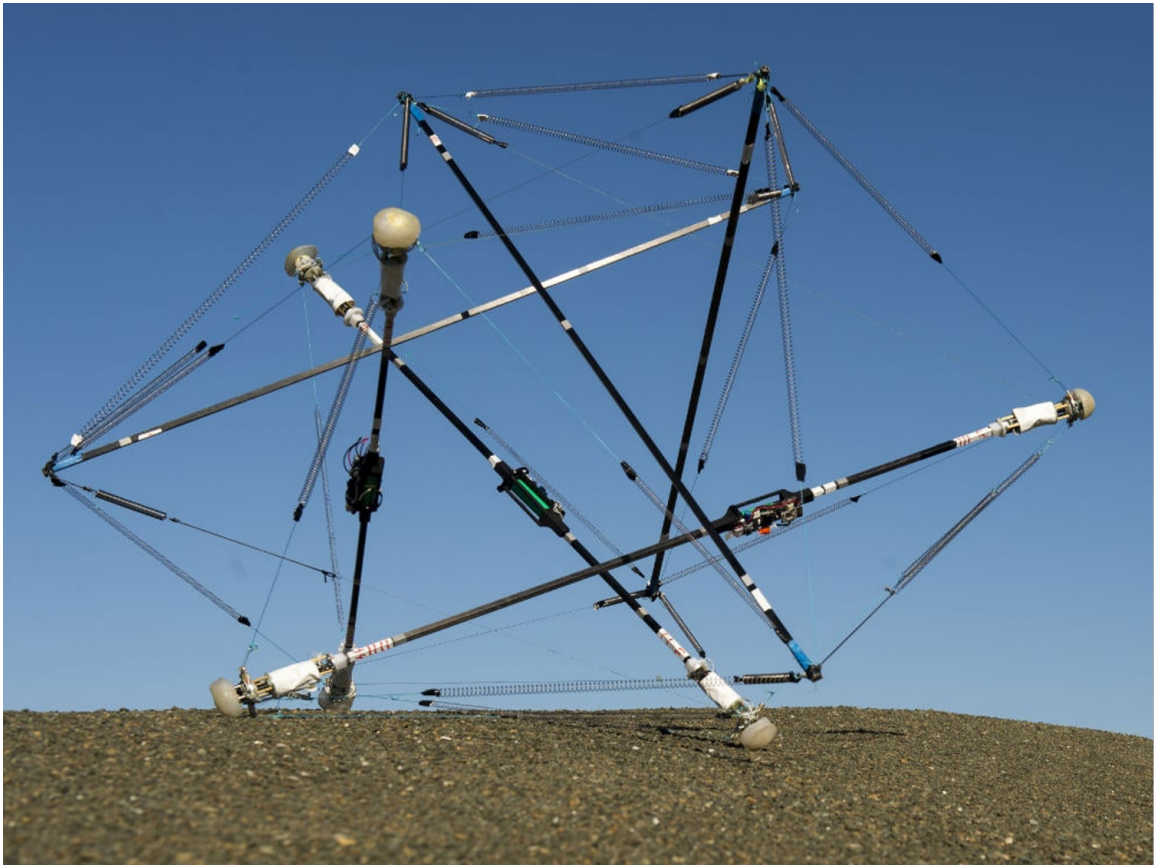


Figure 1.3. NASA Super Ball Bot [26]

1.2 Objectives

To facilitate the emergence of space-based tensegrity robotic systems, this thesis focuses on the development and implementation of a model-based tensegrity shape control law. In support of this objective, the main elements of this thesis are as follows.

1. Develop a single matrix differential equation to simulate the multi-body dynamics of tensegrity systems in non-minimal coordinates
2. Implement a model-based shape control law that uses state feedback to control the shape of a tensegrity structure
3. Utilize the concept of self-similar iterations to design a dexterous tensegrity robotic arm
4. Simulate the deployment of a novel tensegrity robotic arm

1.3 Definitions

Tensegrity structures are axially loaded compressive members (bars or struts) that are stabilized by a network of tensile members (strings or cables) [3]. The nomenclature used to describe compressive and tensile elements often varies from paper to paper. In this manuscript, we refer to the compressive elements as bars and the tensile members as strings.

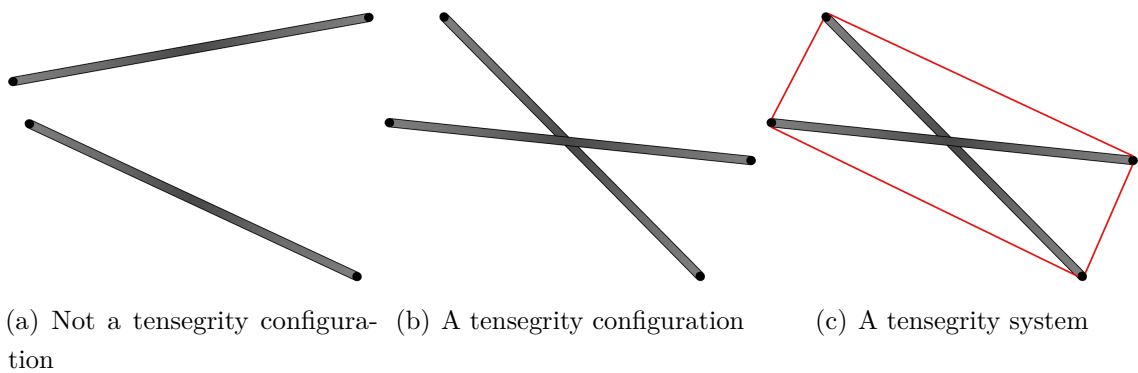


Figure 1.4. Tensegrity definition

We depict bar elements in grey and string elements in red, as portrayed in Figure 1.4. To work towards a more precise engineering definition of tensegrity, we define the

set of positions and orientations of all rigid bodies in the structure as the tensegrity's *configuration*. On the other hand, we refer to the set of connections between bars and strings as the tensegrity's *connectivity*.

Definition. We say that the configuration of rigid bodies is a *tensegrity configuration* if there exists a string *connectivity* able to stabilize the configuration [3].

As a subset for illustration, notice that the collection of bar elements in Figure 1.4(a) is not a tensegrity *configuration* as there is no string *connectivity* to stabilize the two bars. On the other hand, the collection of bars in Figure 1.4(b) is called a tensegrity *configuration* because one could attach strings around the outer perimeter to stabilize the structure. Once strings are added to stabilize the *configuration*, it is referred to as a *tensegrity system*, as depicted in Figure 1.4(c).

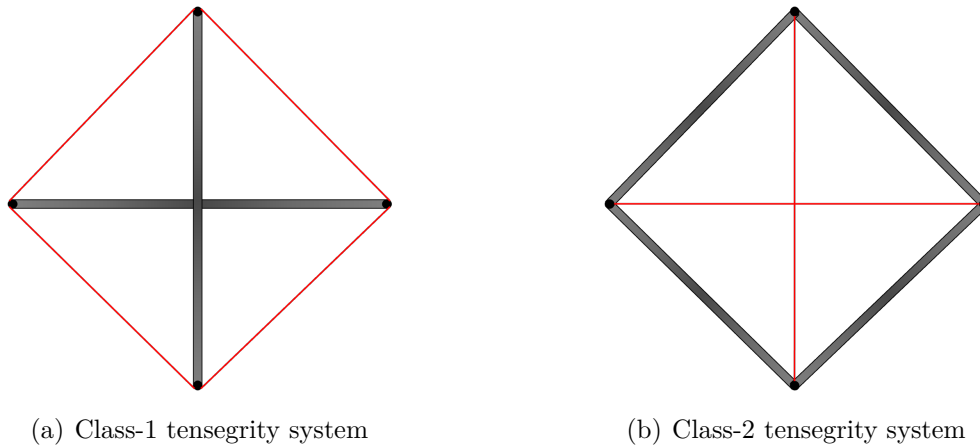


Figure 1.5. Tensegrity classification

To further distinguish between the different types of systems which fit this definition, we add one more distinction.

Definition. A tensegrity configuration that has no contacts between its rigid bodies is a Class-1 tensegrity system, and a tensegrity system with as many as k rigid bodies in contact is a Class- k tensegrity system [3].

Figure 1.5(a) depicts a Class-1 tensegrity system, commonly known as the T-bar, while Figure 1.5(b) depicts a Class-2 system known as the D-bar. One may question, at first, why the definition of tensegrity must be so precise. As we will later see, the design and optimization of tensegrity systems relies very heavily on precise mathematical definition.

1.4 Overview

This thesis is organized as follows. In Chapter 2, we derive a computationally efficient nonlinear dynamic model to simulate tensegrity system dynamics. To simplify the governing equations, a non-minimal coordinate system is used to locate each bar member (6 degrees of freedom for each bar instead of 5). This allows us to formulate Class-1 tensegrity system dynamics as a compact matrix differential equation. Through the use of connectivity matrices, we exploit the tensegrity’s mathematical structure, which reduces computational errors in the numerical simulation. Then, we modify the equations of motion to account for Class-k structures by modeling bar contact forces. A reduced-order model is provided to solve for the bar contact forces analytically. At the end of the chapter, simulation results are provided to verify the Class-1 and Class-k equations of motion.

In Chapter 3, we design a model-based shape control law that uses state feedback to control the shape of a tensegrity structure. This is done by utilizing the dynamics model from Chapter 2 to regulate the error dynamics about a nominal state trajectory. We define the control variable as the force density in each string. This allows the equations of motion to be written in control-affine form. Leveraging concepts from Lyapunov theory, we assess the system stability and then formulate a second order matrix differential equation in the error dynamics. Then, we pose the control law as a linear algebra problem that can be used to solve for the required string force density at each time step. The physical control variable (string tensions) can be obtained with a nonlinear transformation. We discuss several important considerations to guarantee feasible solutions for the required string tensions. At the end of Chapter 3, we verify the control law for Class-1 and Class-K tensegrity systems by simulating the position control of basic T-bar and D-bar structures.

Finally, in Chapter 4, a novel robotic arm is developed by combining our results from the basic T-bar and D-bar structures. We introduce the concept of self-similar iterations to design compressive structures of increasing complexity. Several design considerations are discussed, such as optimizing the mass or dexterity of the structure. A new robotic arm is designed by replacing the horizontal compressive elements of the T-bar with basic D-bar structures. In this chapter, we introduce the 3-dimensional analogues of the T-bar and D-bar structures. This enables the design and simulation of physically realizable structures. At the end of the chapter, we simulate the robotic arm’s extension by regulating certain node coordinates to nominal reference trajectories. Our simulation

proves that the dynamic model and control framework can be used to seamlessly design, analyze, and control complex tensegrity structures.

In Chapter 5, suggestions for future work are presented. We provide a brief overview of an experimental tensegrity testbed that uses computer vision to track nodes in the structure. Several considerations are discussed for the physical control of a cylindrical triplex tensegrity. We also discuss shortcomings and present avenues for future research in the optimal control and robust control of tensegrity systems.

Chapter 2 | Tensegrity System Dynamics

We begin this chapter by developing a vector-based approach to model tensegrity system dynamics, closely following recent developments made by Goyal and Skelton [20]. Starting with Class-1 systems, we generalize the dynamics of a single bar element subject to arbitrary forces at its endpoints. Then, connectivity matrices are defined and introduced to locate each bar member in a non-minimal coordinate system (6 degrees of freedom for each bar instead of 5). By making use of the connectivity matrices, we formalize the internal tension network acting throughout the string elements. To verify the dynamics model, we simulate the free response of a basic tensegrity structure known as the T-bar.

Furthermore, we extend the Class-1 dynamics model to handle Class-k tensegrity systems. In Class-k systems, multiple bar members meet at a single node, causing contact forces to arise. To model these contact forces, we introduce a geometric constraint equation and solve analytically for the Lagrange multipliers which satisfy this constraint. The Class-1 dynamics equation is then modified with the added constraint forces. To verify the Class-k dynamics model, we simulate the free response of a simple D-bar tensegrity structure. Then, a case study is done on the double pendulum to compare this approach to the Lagrangian dynamics formulation in minimal coordinates.

2.1 Vector Notation

Owing to their network of strings and bars, tensegrity structures are very well suited for the rich field of vector analysis. In this approach, we employ Gibbs vector notation [31] and represent three-dimensional objects with magnitude and direction in boldface script. For example, the Gibbs vector \mathbf{v} can be described in any reference frame. In a specified reference frame, the components of the Gibbs vector \mathbf{v} are denoted by a 3×1 matrix $\mathbf{v} = [v_1 \ v_2 \ v_3]^T$.

A vector can be defined in multiple reference frames and we represent a reference frame by a 3×3 vectrix [32] $\mathcal{E} \equiv [\hat{\mathbf{e}}_1 \ \hat{\mathbf{e}}_2 \ \hat{\mathbf{e}}_3]$ where $\hat{\mathbf{e}}_i$ ($i = 1, 2, 3$) form a right-handed set of basis vectors for which

$$\begin{aligned}\hat{\mathbf{e}}_i \cdot \hat{\mathbf{e}}_j &= 0 \ \forall i \neq j \\ \hat{\mathbf{e}}_i \cdot \hat{\mathbf{e}}_j &= 1 \ \forall i = j \\ \hat{\mathbf{e}}_i \times \hat{\mathbf{e}}_j &= \hat{\mathbf{e}}_k \ \forall (i, j, k) = \{(1, 2, 3), (2, 3, 1), (3, 1, 2)\}.\end{aligned}$$

For two vectors described in the same frame ($\mathbf{a} = \mathcal{E}\mathbf{a}^\mathcal{E}$ and $\mathbf{b} = \mathcal{E}\mathbf{b}^\mathcal{E}$), it is convenient to define the dot and cross products in component form as

$$\begin{aligned}\mathbf{a} \cdot \mathbf{b} &= (\mathcal{E}\mathbf{a}^\mathcal{E}) \cdot (\mathcal{E}\mathbf{b}^\mathcal{E}) = \mathbf{a}^{\mathcal{E}T} (\mathcal{E}^T \cdot \mathcal{E}) \mathbf{b}^\mathcal{E} = \mathbf{a}^{\mathcal{E}T} \mathbf{b}^\mathcal{E} \\ \mathbf{a} \times \mathbf{b} &= (\mathcal{E}\mathbf{a}^\mathcal{E}) \times (\mathcal{E}\mathbf{b}^\mathcal{E}) = \mathcal{E}\tilde{\mathbf{a}}^\mathcal{E}\mathbf{b}^\mathcal{E}\end{aligned}$$

where

$$\tilde{\mathbf{a}}^\mathcal{E} = \begin{bmatrix} 0 & -a_3^\mathcal{E} & a_2^\mathcal{E} \\ a_3^\mathcal{E} & 0 & -a_1^\mathcal{E} \\ -a_2^\mathcal{E} & a_1^\mathcal{E} & 0 \end{bmatrix}$$

is the skew-symmetric matrix from the three components of $\mathbf{a}^\mathcal{E}$.

2.2 Vector Kinematics

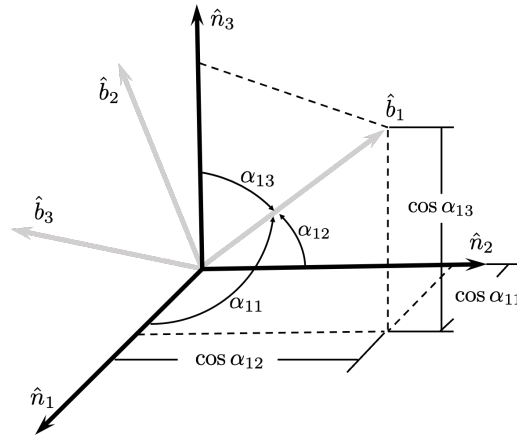


Figure 2.1. Direction cosines

Let us consider two reference frames, $\mathcal{N} \equiv [\hat{\mathbf{n}}_1 \ \hat{\mathbf{n}}_2 \ \hat{\mathbf{n}}_3]$ and $\mathcal{B} \equiv [\hat{\mathbf{b}}_1 \ \hat{\mathbf{b}}_2 \ \hat{\mathbf{b}}_3]$, where \mathcal{N} is a global, inertial, reference frame and \mathcal{B} is a body-fixed reference frame attached to an arbitrary bar member. Then, a vector can be represented with components in both of these frames as:

$$\begin{aligned}\mathbf{v} &= \mathcal{N}\mathbf{v}^{\mathcal{N}} \\ &= \mathcal{B}\mathbf{v}^{\mathcal{B}}\end{aligned}$$

which implies

$$\mathbf{v}^{\mathcal{B}} = (\mathcal{B}^T \mathcal{N})\mathbf{v}^{\mathcal{N}} = \mathcal{C}^{\mathcal{B}\mathcal{N}}\mathbf{v}^{\mathcal{N}}$$

where we define $\mathcal{C}^{\mathcal{B}\mathcal{N}}$ as the Direction Cosine Matrix (DCM) [33] which maps vector components in the inertial frame to the body-fixed frame. The two frames are depicted in Figure 2.1. Let the angles α_{1i} be the angles formed between the first body vector $\hat{\mathbf{b}}_1$ and the three inertial basis vectors $\hat{\mathbf{n}}_1, \hat{\mathbf{n}}_2$ and $\hat{\mathbf{n}}_3$. The cosines of these angles are referred to as the direction cosines of the vector $\hat{\mathbf{b}}_1$ relative to the frame \mathcal{N} . To illustrate, the unit vector $\hat{\mathbf{b}}_1$ can be projected onto the inertial reference frame \mathcal{N} as

$$\hat{\mathbf{b}}_1 = \cos \alpha_{11} \hat{\mathbf{n}}_1 + \cos \alpha_{12} \hat{\mathbf{n}}_2 + \cos \alpha_{13} \hat{\mathbf{n}}_3. \quad (2.1)$$

Put simply, the direction cosines $\cos \alpha_{1j}$ are the orthogonal components of the vector $\hat{\mathbf{b}}_1$ on the inertial reference frame. Similarly, we have the orthogonal projections

$$\hat{\mathbf{b}}_2 = \cos \alpha_{21} \hat{\mathbf{n}}_1 + \cos \alpha_{22} \hat{\mathbf{n}}_2 + \cos \alpha_{23} \hat{\mathbf{n}}_3. \quad (2.2)$$

$$\hat{\mathbf{b}}_3 = \cos \alpha_{31} \hat{\mathbf{n}}_1 + \cos \alpha_{32} \hat{\mathbf{n}}_2 + \cos \alpha_{33} \hat{\mathbf{n}}_3. \quad (2.3)$$

Combining Eqs. (2.1)-(2.3), the vectrix $\mathcal{B} = [\hat{\mathbf{b}}_1 \ \hat{\mathbf{b}}_2 \ \hat{\mathbf{b}}_3]$ can be compactly expressed as

$$\mathcal{B}^T = \begin{bmatrix} \cos \alpha_{11} & \cos \alpha_{12} & \cos \alpha_{13} \\ \cos \alpha_{21} & \cos \alpha_{22} & \cos \alpha_{23} \\ \cos \alpha_{31} & \cos \alpha_{32} & \cos \alpha_{33} \end{bmatrix} \mathcal{N}^T = \mathcal{C}^{\mathcal{B}\mathcal{N}} \mathcal{N}^T$$

Taking the transpose,

$$\mathcal{B} = \mathcal{N} \mathcal{C}^{\mathcal{N}\mathcal{B}}$$

where $\mathcal{C}^{\mathcal{N}\mathcal{B}} = \mathcal{C}^{\mathcal{B}\mathcal{N}T}$. It is also convenient to specify the inertial velocity of a vector \mathbf{v} as

$$\dot{\mathbf{v}} = \dot{\mathcal{B}}\mathbf{v}^{\mathcal{B}} + \mathcal{B}\dot{\mathbf{v}}^{\mathcal{B}} = \mathcal{B}[\tilde{\boldsymbol{\omega}}^{\mathcal{B}}\mathbf{v}^{\mathcal{B}} + \dot{\mathbf{v}}^{\mathcal{B}}]. \quad (2.4)$$

where $\boldsymbol{\omega}$ is the angular velocity of frame \mathcal{B} with respect to frame \mathcal{N} and we have applied the transport theorem [33] to take the time rate of change of the non-inertial reference frame \mathcal{B} .

2.3 Dynamics of a Single Bar

Tensegrity systems comprise a set of bars connected by an internal tension network. As a step toward developing the equations of motion for an entire tensegrity system, we will first generalize the dynamics of a single bar element. For Class-1 systems, internal forces are applied throughout the network via string tensions. When we later consider Class-k systems, we must also account for bar contact forces. To simplify our preliminary developments, we will consider forces acting at the bar ends to be arbitrary.

2.3.1 Rotational Dynamics

To begin, consider a vector \mathbf{b} along an arbitrary bar member of length $l = \|\mathbf{b}\|$, as depicted in Figure 2.2. The vector \mathbf{r} locates the center of mass of the bar. Let the body-fixed reference frame \mathcal{B} be aligned with the bar such that $\hat{\mathbf{b}}_3$ is parallel to the bar vector \mathbf{b} .

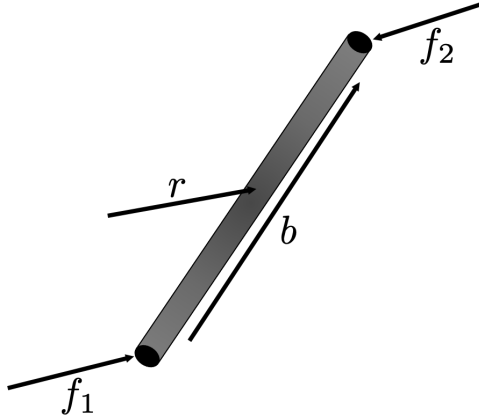


Figure 2.2. A single bar member

In body coordinates, the bar vector \mathbf{b} is described as

$$\mathbf{b} = \mathcal{B}\mathbf{b}^{\mathcal{B}}, \quad \mathbf{b}^{\mathcal{B}} = [0 \ 0 \ l]^T. \quad (2.5)$$

Applying Eq. (2.4) to Eq. (2.5), the inertial velocity of the bar vector, described in body coordinates, is

$$\dot{\mathbf{b}} = \dot{\mathcal{B}}\mathbf{b}^{\mathcal{B}} + \mathcal{B}\dot{\mathbf{b}}^{\mathcal{B}} = \dot{\mathcal{B}}\mathbf{b}^{\mathcal{B}} = \mathcal{B}\tilde{\omega}^{\mathcal{B}}\mathbf{b}^{\mathcal{B}} \quad (2.6)$$

where we have applied $\dot{\mathbf{b}}^{\mathcal{B}} = 0$ due to the constant length of the bar.

Now, the angular momentum of a bar about its center of mass is

$$\mathbf{h}_b = I_b\boldsymbol{\omega}_b \quad (2.7)$$

where $\boldsymbol{\omega}_b$ and I_b are the angular velocity and moment of inertia of the bar, respectively. Our goal is to represent Eq. (2.7) in terms of the bar vector \mathbf{b} and the bar velocity vector $\dot{\mathbf{b}}$. To this end, it is useful to compute $\mathbf{b} \times \dot{\mathbf{b}}$ as

$$\begin{aligned} \mathbf{b} \times \dot{\mathbf{b}} &= (\mathcal{B}\mathbf{b}^{\mathcal{B}}) \times (\mathcal{B}\tilde{\omega}^{\mathcal{B}}\mathbf{b}^{\mathcal{B}}) \\ &= \mathcal{B}\tilde{\mathbf{b}}^{\mathcal{B}}\tilde{\omega}^{\mathcal{B}}\mathbf{b}^{\mathcal{B}} = -\mathcal{B}\tilde{\mathbf{b}}^{\mathcal{B}}\tilde{\mathbf{b}}^{\mathcal{B}}\omega^{\mathcal{B}} = -\mathcal{B}(\tilde{\mathbf{b}}^{\mathcal{B}})^2\omega^{\mathcal{B}} \end{aligned} \quad (2.8)$$

Now, using the identity

$$(\tilde{\mathbf{b}}^{\mathcal{B}})^2 = -(\mathbf{b}^{\mathcal{B}T}\mathbf{b}^{\mathcal{B}}I_3 - \mathbf{b}^{\mathcal{B}}\mathbf{b}^{\mathcal{B}T}), \quad (2.9)$$

where, in general, I_n is the $n \times n$ identity matrix, Eq. (2.8) becomes

$$\mathbf{b} \times \dot{\mathbf{b}} = \mathcal{B}\left(\|\mathbf{b}^{\mathcal{B}}\|^2 I_3 - \mathbf{b}^{\mathcal{B}}\mathbf{b}^{\mathcal{B}T}\right)\omega^{\mathcal{B}} \quad (2.10)$$

Recalling that $\mathbf{b}^{\mathcal{B}} = [0 \ 0 \ l]^T$ and $l = \|\mathbf{b}^{\mathcal{B}}\|$, Eq. (2.10) can be further simplified as

$$\begin{aligned} \mathbf{b} \times \dot{\mathbf{b}} &= \mathcal{B}\left(\begin{bmatrix} l^2 & 0 & 0 \\ 0 & l^2 & 0 \\ 0 & 0 & l^2 \end{bmatrix} - \begin{bmatrix} 0 & 0 & 0 \\ 0 & 0 & 0 \\ 0 & 0 & l^2 \end{bmatrix}\right)\omega^{\mathcal{B}} \\ &= \mathcal{B}\begin{bmatrix} l^2 & 0 & 0 \\ 0 & l^2 & 0 \\ 0 & 0 & 0 \end{bmatrix}\omega^{\mathcal{B}} = \mathcal{B}l^2\begin{bmatrix} \omega_1^{\mathcal{B}} \\ \omega_2^{\mathcal{B}} \\ 0 \end{bmatrix} = \|\mathbf{b}\|^2\boldsymbol{\omega}_b \end{aligned}$$

In summary, the relationship between $\boldsymbol{\omega}_b$, the angular velocity of bar \mathbf{b} , and the vectors \mathbf{b} and $\dot{\mathbf{b}}$ is

$$\boldsymbol{\omega}_b = \frac{\mathbf{b} \times \dot{\mathbf{b}}}{\|\mathbf{b}\|^2} \quad (2.11)$$

This result is also shown in [34]. Substituting Eq. (2.11) into Eq. (2.7), the angular momentum of bar \mathbf{b} about its mass center is:

$$\begin{aligned}\mathbf{h} &= \mathbf{h}_b = I_b \boldsymbol{\omega}_b \\ &= \left(\frac{m_b l^2}{12} + \frac{m_b r_b^2}{4} \right) \left(\frac{\mathbf{b} \times \dot{\mathbf{b}}}{l^2} \right) \\ &= \left(\frac{m_b}{12} + \frac{m_b r_b^2}{4l^2} \right) \mathbf{b} \times \dot{\mathbf{b}} = J \mathbf{b} \times \dot{\mathbf{b}}\end{aligned}$$

where r_b is the radius of the bar and $J = \frac{m_b}{12} + \frac{m_b r_b^2}{4l^2}$. It is also useful to compute the time derivative of the angular momentum as

$$\begin{aligned}\dot{\mathbf{h}} &= J \dot{\mathbf{b}} \times \dot{\mathbf{b}} + J \mathbf{b} \times \ddot{\mathbf{b}} \\ &= J \mathbf{b} \times \ddot{\mathbf{b}}\end{aligned}\tag{2.12}$$

Now, the law of conservation of angular momentum states that the time derivative of the bar's angular momentum vector \mathbf{h} is equal to the sum of torques $\boldsymbol{\tau}$ acting about the bar's center of mass. As illustrated in Figure 2.2, we consider two arbitrary forces, \mathbf{f}_1 and \mathbf{f}_2 , acting on opposite ends of the bar member. The resulting conservation equation, written in terms of the bar vector \mathbf{b} is

$$\begin{aligned}\dot{\mathbf{h}} &= \boldsymbol{\tau} \\ &= \frac{1}{2} \mathbf{b} \times (\mathbf{f}_2 - \mathbf{f}_1)\end{aligned}\tag{2.13}$$

Combining Eqs. (2.12) and (2.13) yields

$$J \mathbf{b} \times \ddot{\mathbf{b}} = \frac{1}{2} \mathbf{b} \times (\mathbf{f}_2 - \mathbf{f}_1),\tag{2.14}$$

which describes the rotational dynamics of a bar member subject to arbitrary forces at its end points. In fact, Eq. (2.14) is well known to describe the rotational dynamics of truss elements and can be checked in [35, 36]. Eq. (2.14) can be written in any coordinates. However, to simplify the final equations of motion, we choose to write it in inertial coordinates and hereafter define $\mathbf{b} = \mathbf{b}^N$. Now, we can write Eq. (2.14) as

$$J \tilde{\mathbf{b}} \ddot{\mathbf{b}} = \frac{1}{2} \tilde{\mathbf{b}} (\mathbf{f}_2 - \mathbf{f}_1),\tag{2.15}$$

So far, we have chosen to represent a bar member as a vector in a global, non-minimal, coordinate system. In order to ensure that the magnitude of the bar vector, $\|\mathbf{b}\|$, remains

constant with its length l , a constant length constraint must be imposed on the rotational dynamics:

$$\mathbf{b}^T \mathbf{b} = l^2 \quad (2.16)$$

Now, the goal is to augment the rotational dynamics of Eq. (2.15) with the constant length constraint. Differentiating Eq. (2.16) twice:

$$\begin{aligned} \dot{\mathbf{b}}^T \mathbf{b} + \mathbf{b}^T \dot{\mathbf{b}} &= 0 = 2\mathbf{b}^T \dot{\mathbf{b}} \\ \dot{\mathbf{b}}^T \dot{\mathbf{b}} + \mathbf{b}^T \ddot{\mathbf{b}} &= 0 \\ \mathbf{b}^T \ddot{\mathbf{b}} &= -\dot{\mathbf{b}}^T \dot{\mathbf{b}} \end{aligned} \quad (2.17)$$

Having reformulated the constant bar length constraint in terms of $\ddot{\mathbf{b}}$, the rotational dynamics (Eq. (2.15)) and the new length constraint (Eq. (2.17)) can be combined in matrix form as

$$\begin{bmatrix} \tilde{\mathbf{b}} \\ \mathbf{b}^T \end{bmatrix} \ddot{\mathbf{b}} = \begin{bmatrix} \frac{1}{2J} \tilde{\mathbf{b}} (\mathbf{f}_2 - \mathbf{f}_1) \\ -\dot{\mathbf{b}}^T \dot{\mathbf{b}} \end{bmatrix}, \quad (2.18)$$

which results in a single linear algebra problem that can be solved for $\ddot{\mathbf{b}}$. By inspection of Eq. (2.18), one can verify the existence condition for a solution and the full rank of the matrix multiplying $\ddot{\mathbf{b}}$. Denoting the pseudoinverse by the \dagger superscript, the unique solution for $\ddot{\mathbf{b}}$ is

$$\begin{aligned} \ddot{\mathbf{b}} &= \begin{bmatrix} \tilde{\mathbf{b}} \\ \mathbf{b}^T \end{bmatrix}^\dagger \begin{bmatrix} \frac{1}{2J} \tilde{\mathbf{b}} (\mathbf{f}_2 - \mathbf{f}_1) \\ -\dot{\mathbf{b}}^T \dot{\mathbf{b}} \end{bmatrix} \\ &= \frac{1}{l^2} \begin{bmatrix} -\tilde{\mathbf{b}} & \mathbf{b} \end{bmatrix} \begin{bmatrix} \frac{1}{2J} \tilde{\mathbf{b}} (\mathbf{f}_2 - \mathbf{f}_1) \\ -\dot{\mathbf{b}}^T \dot{\mathbf{b}} \end{bmatrix} \\ &= \frac{1}{l^2} \begin{bmatrix} -\frac{1}{2J} \tilde{\mathbf{b}} \tilde{\mathbf{b}} (\mathbf{f}_2 - \mathbf{f}_1) - \mathbf{b} \dot{\mathbf{b}}^T \dot{\mathbf{b}} \end{bmatrix} \\ &= -\frac{1}{2Jl^2} \left(-l^2 I_3 + \mathbf{b} \mathbf{b}^T \right) (\mathbf{f}_2 - \mathbf{f}_1) - \frac{1}{l^2} \mathbf{b} \dot{\mathbf{b}}^T \dot{\mathbf{b}} \end{aligned} \quad (2.19)$$

where we have used the identity of Eq. (2.9). Rearranging Eq. (2.19) yields the complete rotational dynamics of a single bar member including the length constraint:

$$J \ddot{\mathbf{b}} = \frac{1}{2} (\mathbf{f}_2 - \mathbf{f}_1) - \frac{1}{2l^2} \mathbf{b} \mathbf{b}^T (\mathbf{f}_2 - \mathbf{f}_1) - \frac{J}{l^2} \mathbf{b} \dot{\mathbf{b}}^T \dot{\mathbf{b}} \quad (2.20)$$

2.3.2 Translational Dynamics

Returning our attention to Figure 2.2, a single bar element of mass m_b is represented as a vector \mathbf{b} with its center of mass located by the vector \mathbf{r} . Two arbitrary forces, \mathbf{f}_1 and \mathbf{f}_2 , act on opposite ends of the bar. From Newton's 2nd Law, the sum of these forces influence the inertial acceleration of the bar's mass center as

$$m_b \ddot{\mathbf{r}} = \mathbf{f}_1 + \mathbf{f}_2, \quad (2.21)$$

which can be written in any coordinate system. To simplify the final equations of motion, we choose to write Eq. (2.21) in inertial coordinates.

2.4 Matrix Formulation of Tensegrity Dynamics

Together, Eqn. (2.20) and Eqn. (2.21) govern the dynamics of any bar member in a classical tensegrity structure. Consequently, a full tensegrity structure comprising β bar members would yield 2β vector equations to describe the system dynamics. The classic multibody dynamics approach to formulating the governing equations would stack these equations into a single vector [35]. However, a more compact approach exists for modeling tensegrity structures that exploits their unique topology. In this section, connectivity matrices are introduced to describe tensegrity system dynamics with a single matrix differential equation.

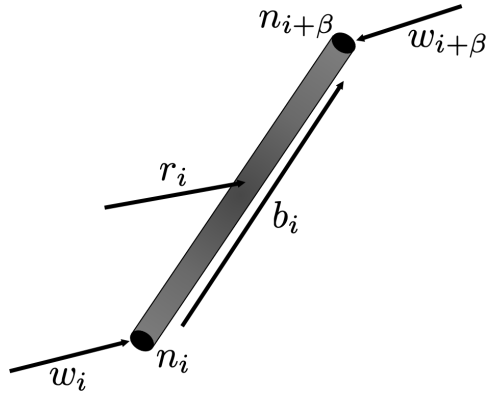


Figure 2.3. Numbering convention of a single bar

Consider a full tensegrity structure comprising β bar members and α string members. We define a $3 \times 2\beta$ node matrix $N = [\mathbf{n}_1 \ \mathbf{n}_2 \ \cdots \ \mathbf{n}_{2\beta}]$ which appends the inertial components of the node vectors \mathbf{n}_i . Similarly, we define the $3 \times \beta$ matrix of bar vectors

$B = [\mathbf{b}_1 \ \mathbf{b}_2 \ \cdots \ \mathbf{b}_\beta]$ and the $3 \times \alpha$ matrix of string vectors $S = [\mathbf{s}_1 \ \mathbf{s}_2 \ \cdots \ \mathbf{s}_\alpha]$ from the inertial components of \mathbf{b}_i and \mathbf{s}_i , respectively. By convention, we define the matrix of nodes at the base of each bar member as $N_1 = [\mathbf{n}_1 \ \mathbf{n}_2 \ \cdots \ \mathbf{n}_\beta]$ and the matrix of nodes at the terminal ends is defined as $N_2 = [\mathbf{n}_{1+\beta} \ \mathbf{n}_{2+\beta} \ \cdots \ \mathbf{n}_{2\beta}]$. By this convention, a tensegrity structure with $n = 2\beta$ nodes yields the $3 \times n$ node matrix $N = [N_1 \ N_2]$.

In short, connectivity matrices are used to relate the matrix of bar members B and the matrix of string members S to the node matrix N . By inspecting the network, one can immediately define connectivity matrices C_b and C_s with appropriate elements (0,1,-1) such that $B = NC_b^T$ and $S = NC_s^T$. To illustrate, consider the bar member numbering convention depicted in Figure 2.3. The bar vector \mathbf{b}_i could be written in terms of the node vectors as $\mathbf{b}_i = \mathbf{n}_{i+\beta} - \mathbf{n}_i$. For the node matrix $N = [N_1 \ N_2]$, the above convention yields $C_b = [-I_\beta \ I_\beta]$. In general, C_b is a $\beta \times n$ matrix in which the rows specify the connectivity of each bar member. Now, the vector locating the center of mass of the bar member in Figure 2.3 is $\mathbf{r}_i = \mathbf{n}_i + \frac{1}{2}\mathbf{b}_i$. By the above convention, we define the matrix

$$\begin{aligned} R &= N_1 + \frac{1}{2}B \\ &= N_1 + \frac{1}{2}(N_2 - N_1) \\ &= N \frac{1}{2} \begin{bmatrix} I_\beta \\ I_\beta \end{bmatrix} = NC_r^T \end{aligned} \tag{2.22}$$

Now that we have defined the connectivity matrices, C_b , C_s , and C_r , the next step is to extend the dynamics of Eq. (2.20) to include the rotational dynamics of each bar member. To begin, we append the rotational dynamics of the i^{th} bar member in Eq. (2.20) to the i^{th} column of the matrix $\ddot{B}\hat{J}$ as

$$\ddot{B}\hat{J} = \begin{bmatrix} \ddot{\mathbf{b}}_1 & \ddot{\mathbf{b}}_2 & \cdots & \ddot{\mathbf{b}}_\beta \end{bmatrix} \begin{bmatrix} J_1 & 0 & \cdots & 0 \\ 0 & J_2 & \cdots & 0 \\ \vdots & \vdots & \ddots & \vdots \\ 0 & 0 & \cdots & J_\beta \end{bmatrix} = \begin{bmatrix} J_1 \ddot{\mathbf{b}}_1 & J_2 \ddot{\mathbf{b}}_2 & \cdots & J_\beta \ddot{\mathbf{b}}_\beta \end{bmatrix} \tag{2.23}$$

where the $\{\hat{\cdot}\}$ operator forms a diagonal matrix from the elements of a vector. Similarly, we can extend the terms on the right hand side of Eq. (2.20) to include the rotational dynamics of every bar in the structure. Proceeding, we define the force matrix F whose

i^{th} column is the total force vector acting on the i^{th} node, including both internal forces from string tensions and external forces. Hence, the terms on the right hand side of Eq. (2.20) can be rewritten for the i^{th} bar as

$$\frac{1}{2}(\mathbf{f}_{2_i} - \mathbf{f}_{1_i}) = \frac{1}{2} [FC_b^T]_i, \quad (2.24)$$

$$-\frac{1}{2l_i^2} \mathbf{b}_i \mathbf{b}_i^T (\mathbf{f}_{2_i} - \mathbf{f}_{1_i}) = -\frac{1}{2} [B\hat{\mathbf{l}}^{-2} [B^T FC_b^T]]_i, \quad (2.25)$$

$$-\frac{J_i}{l_i^2} \mathbf{b}_i \dot{\mathbf{b}}_i^T \dot{\mathbf{b}}_i = - [B\hat{\mathbf{J}}\hat{\mathbf{l}}^{-2} [\dot{B}^T \dot{B}]]_i. \quad (2.26)$$

where the $[\circ]$ operator sets every off-diagonal element of the square matrix to zero. Combining Eqs. (2.23)-(2.26) leads to a single matrix expression describing the rotational dynamics of every bar member in a tensegrity structure:

$$\ddot{B}\hat{\mathbf{J}} = \frac{1}{2} FC_b^T - \frac{1}{2} B\hat{\mathbf{l}}^{-2} [B^T FC_b^T] - B\hat{\mathbf{J}}\hat{\mathbf{l}}^{-2} [\dot{B}^T \dot{B}] \quad (2.27)$$

We can further simplify Eq. (2.27) by defining $\hat{\boldsymbol{\lambda}}$ to emphasize the influence of the bar length constraint:

$$\hat{\boldsymbol{\lambda}} = -\hat{\mathbf{J}}\hat{\mathbf{l}}^{-2} [\dot{B}^T \dot{B}] - \frac{1}{2} \hat{\mathbf{l}}^{-2} [B^T FC_b^T], \quad (2.28)$$

$$\ddot{B}\hat{\mathbf{J}} = \frac{1}{2} FC_b^T + B\hat{\boldsymbol{\lambda}}. \quad (2.29)$$

The next step is to extend the translational dynamics of Eq. (2.21) into a matrix expression for the entire structure. Using Eq. (2.22), we can write the translational dynamics of the i^{th} bar as

$$\mathbf{m}_{b_i} \ddot{\mathbf{r}}_i = \mathbf{f}_{1_i} + \mathbf{f}_{2_i} = [\ddot{R}\hat{\mathbf{m}}_b]_i = 2 [FC_r^T]_i, \quad (2.30)$$

which leads to the matrix expression for the translational dynamics of every bar member:

$$\ddot{R}\hat{\mathbf{m}}_b = 2FC_r^T. \quad (2.31)$$

Now, the matrix expressions for rotational and translational dynamics (Eqn. (2.29) and Eqn. (2.31), respectively) can be combined into a single matrix expression as

$$\begin{bmatrix} \ddot{B} & \ddot{R} \end{bmatrix} \begin{bmatrix} \hat{\mathbf{J}} & 0 \\ 0 & \hat{\mathbf{m}}_b \end{bmatrix} + \begin{bmatrix} B & R \end{bmatrix} \begin{bmatrix} -\hat{\lambda} & 0 \\ 0 & 0 \end{bmatrix} = F \begin{bmatrix} \frac{1}{2}C_b^T & 2C_r^T \end{bmatrix}. \quad (2.32)$$

Taking the inverse $\begin{bmatrix} \frac{1}{2}C_b^T & 2C_r^T \end{bmatrix}^{-1} = \begin{bmatrix} C_b^T & C_r^T \end{bmatrix}^T$ [37], Eq. (2.32) can be rewritten as

$$\begin{aligned} \begin{bmatrix} \ddot{B} & \ddot{R} \end{bmatrix} \begin{bmatrix} \hat{\mathbf{J}} & 0 \\ 0 & \hat{\mathbf{m}}_b \end{bmatrix} \begin{bmatrix} C_b \\ C_r \end{bmatrix} + \begin{bmatrix} B & R \end{bmatrix} \begin{bmatrix} -\hat{\lambda} & 0 \\ 0 & 0 \end{bmatrix} \begin{bmatrix} C_b \\ C_r \end{bmatrix} &= F, \\ \begin{bmatrix} \ddot{B} & \ddot{R} \end{bmatrix} \begin{bmatrix} \hat{\mathbf{J}}C_b \\ \hat{\mathbf{m}}_b C_r \end{bmatrix} + \begin{bmatrix} B & R \end{bmatrix} \begin{bmatrix} -\hat{\lambda}C_b \\ 0 \end{bmatrix} &= F. \end{aligned} \quad (2.33)$$

The expressions for bar connectivity and bar center of mass connectivity can be compactly expressed in matrix form as

$$\begin{bmatrix} B & R \end{bmatrix} = N \begin{bmatrix} C_b^T & C_r^T \end{bmatrix} \quad (2.34)$$

Substituting Eq. (2.34) into Eq. (2.33) leads to

$$\ddot{N} \begin{bmatrix} C_b^T & C_r^T \end{bmatrix} \begin{bmatrix} \hat{\mathbf{J}}C_b \\ \hat{\mathbf{m}}_b C_r \end{bmatrix} + N \begin{bmatrix} C_b^T & C_r^T \end{bmatrix} \begin{bmatrix} -\hat{\lambda}C_b \\ 0 \end{bmatrix} = F. \quad (2.35)$$

Carrying out the matrix multiplication in Eq. (2.35) results in a single expression for tensegrity system dynamics in terms of the node matrix N :

$$\ddot{N} \left(C_b^T \hat{\mathbf{J}}C_b + C_r^T \hat{\mathbf{m}}_b C_r \right) - N \left(C_b^T \hat{\lambda}C_b \right) = F. \quad (2.36)$$

Thus far, we have loosely defined the force matrix F such that the i^{th} column corresponds to the total force vector acting on the i^{th} node. Further elaborating, we can subdivide each force vector \mathbf{f}_i into the internal force due to string tension and the external force. Define the external force matrix W such that the i^{th} column corresponds to the external force vector \mathbf{w}_i acting on node \mathbf{n}_i , as depicted in Figure 2.3. The internal forces due to string tension act throughout the string network. Recall that we have defined the string connectivity matrix C_s to satisfy $S = NC_s^T$, where the i^{th} column of S describes the i^{th} string vector \mathbf{s}_i in inertial coordinates. The tension force in the i^{th} string member \mathbf{t}_i acts in equal and opposite directions along \mathbf{s}_i . Therefore, the internal node forces caused by string tensions T is described by TC_s .

To enable control laws that can be developed independently of the material properties of the strings, the control variable is defined as the string ‘force density’ vector $\boldsymbol{\gamma}$ where

each element of $\boldsymbol{\gamma}$ corresponds to the force density in the corresponding string. The tension vector in the i^{th} string is written as $\mathbf{t}_i = \mathbf{s}_i \boldsymbol{\gamma}_i$ (See Appendix A for elastic string modeling). Therefore, the full string tension matrix T can be written as $T = S \hat{\boldsymbol{\gamma}} = N C_s^T \hat{\boldsymbol{\gamma}}$. Then, the internal node forces are described by $N C_s^T \hat{\boldsymbol{\gamma}} C_s$. Combining the internal node forces with the external forces, the full force matrix can be written as

$$F = W - N C_s^T \hat{\boldsymbol{\gamma}} C_s. \quad (2.37)$$

Substituting Eq. (2.37) into Eq. (2.36) leads to

$$\ddot{N} \left(C_b^T \hat{\mathbf{J}} C_b + C_r^T \hat{\mathbf{m}}_b C_r \right) + N \left(C_s^T \hat{\boldsymbol{\gamma}} C_s - C_b^T \hat{\boldsymbol{\lambda}} C_b \right) = W. \quad (2.38)$$

By defining mass and stiffness matrices M and K , we arrive at a single matrix differential equation describing the nonlinear rotational and translational dynamics of a full tensegrity structure:

$$\ddot{N} M + N K = W \quad (2.39a)$$

$$M = C_b^T \hat{\mathbf{J}} C_b + C_r^T \hat{\mathbf{m}}_b C_r, \quad (2.39b)$$

$$K = C_s^T \hat{\boldsymbol{\gamma}} C_s - C_b^T \hat{\boldsymbol{\lambda}} C_b. \quad (2.39c)$$

$$\hat{\boldsymbol{\lambda}} = -\hat{\mathbf{J}} \hat{\mathbf{t}}^{-2} \left[\dot{B}^T \dot{B} \right] - \frac{1}{2} \hat{\mathbf{t}}^{-2} \left[B^T F C_b^T \right]. \quad (2.39d)$$

2.5 Class- k Tensegrity Systems

Class- k tensegrity structures are topologies in which k bar members meet at any given node in the structure [3]. We define the ‘class’ of a tensegrity structure by the maximum number of bar members that meet at any given node in the structure. By convention, Class- k nodes are defined as frictionless ball joints. If there are no ‘bar-to-bar’ joints in a given structure, the structure is said to be Class-1 and the predefined equations of motion (Eqs. (2.39a)-(2.39c)) are valid. If at least one node in a given tensegrity structure connects two bar members, that structure is said to be Class-2, and so on. Due to contact forces at bar-to-bar joints, Eqs. (2.39a)-(2.39c) are not valid for Class- k systems and must be modified.

We proceed by deconstructing each Class- k joint into k Class-1 joints that are constrained to coincide. The geometric constraint can be written as

$$NP = D, \quad (2.40)$$

where $P \in \mathbb{R}^{n \times c}$ and $D \in \mathbb{R}^{3 \times c}$ are specified such that the constrained nodes coincide for c total constraints in the structure. For example, if nodes 1 and 2 are constrained to coincide, one would specify corresponding columns in P and D so that $\mathbf{n}_1 - \mathbf{n}_2 = 0$. Due to the added constraints, the original equations of motion are modified to include contact forces, which can be written as ΩP^T where Ω is the $3 \times c$ matrix of Lagrange multipliers satisfying the dynamics and constraints at all time steps. Based on the developments presented in [20], the added constraint forces are factored into the original dynamics equation to yield the Class- k equations of motion:

$$\ddot{N}M + NK = W + \Omega P^T, \quad (2.41a)$$

$$M = C_b^T \hat{\mathbf{J}} C_b + C_r^T \hat{\mathbf{m}} C_r, \quad (2.41b)$$

$$K = C_s^T \hat{\boldsymbol{\gamma}} C_s - C_b^T \hat{\boldsymbol{\lambda}} C_b, \quad (2.41c)$$

$$\hat{\boldsymbol{\lambda}} = -\hat{\mathbf{J}} \hat{\mathbf{l}}^{-2} [\dot{B}^T \dot{B}] - \frac{1}{2} \hat{\mathbf{l}}^{-2} [B^T (W + \Omega P^T - N C_s^T \hat{\boldsymbol{\gamma}} C_s) C_b^T]. \quad (2.41d)$$

Note that Eq. (2.41d) has been modified to account for the added constraint forces.

2.6 Reduced-order Dynamics

Due to the linear constraints that result from bar contact forces, the motion is restricted in certain dimensions. In other words, the geometric constraints will cause the system dynamics to span a smaller subspace. It is therefore convenient to change the coordinate system to better represent the constrained motion.

To see more clearly why one would desire a change of coordinates, consider the double pendulum system depicted in Figure 2.4. The center of mass of the upper bar could be located in non-minimal (Cartesian) coordinates as (x_1, y_1) . However, because the bar end is pinned at node n_1 , the center of mass of the bar is constrained to a circular trajectory. Therefore, it is more convenient to locate the center of mass of the pinned bar

by its angle from vertical θ_1 . For Class-k tensegrity systems, it is equivalently convenient to represent the constrained motion in a different coordinate system. As we will also see, this approach provides us with a closed-form solution for the matrix of Lagrange constraint multipliers Ω .

To this end, we use the singular value decomposition to factorize the geometric constraint matrix as

$$P = U\Sigma V^T = \begin{bmatrix} U_1 & U_2 \end{bmatrix} \begin{bmatrix} \Sigma_1 \\ 0 \end{bmatrix} \begin{bmatrix} V^T \end{bmatrix} \quad (2.42)$$

where $U \in \mathbb{R}^{n \times n}$ and $V \in \mathbb{R}^{c \times c}$ are orthogonal matrices whose columns are the left- and right-singular vectors of P , respectively, while $\Sigma_1 \in \mathbb{R}^{c \times c}$ is a diagonal matrix of positive singular values. The submatrices $U_1 \in \mathbb{R}^{n \times c}$ and $U_2 \in \mathbb{R}^{n \times (n-c)}$ decompose the vector space that is spanned by P into two lower-dimensional subspaces. We define

$$\eta = [\eta_1 \ \eta_2] \triangleq NU = [NU_1 \ NU_2], \quad (2.43)$$

which transforms the system node vectors into a new space with singular vector basis. Now, the constraint equation (Eq. (2.40)) can be modified as

$$NP = NU\Sigma V^T = \begin{bmatrix} \eta_1 & \eta_2 \end{bmatrix} \begin{bmatrix} \Sigma_1 \\ 0 \end{bmatrix} \begin{bmatrix} V^T \end{bmatrix} = D \quad (2.44)$$

which implies

$$\eta_1 = DV\Sigma_1^{-1}, \quad \dot{\eta}_1 = 0, \quad \ddot{\eta}_1 = 0 \quad (2.45)$$

After applying the transformation, the columns of η_1 span the no-motion space in transformed coordinates and η_2 represents the constrained dynamics in a new coordinate system. Substituting Eqs. (2.42)-(2.45) into Eq. (2.41a) leads to the constrained dynamics:

$$\begin{aligned} \ddot{N}UU^T M + NUU^T K &= W + \Omega V \Sigma^T U^T \\ \ddot{\eta}_2 U_2^T M + \eta_1 U_1^T K + \eta_2 U_2^T K &= W + \Omega V \Sigma^T U^T \end{aligned} \quad (2.46)$$

Post-multiplying Eq. (2.46) by the non-singular matrix $[U_2 M^{-1} U_1]$ will yield two equations, where the first equation is a second order dynamics equation in the reduced coordinates:

$$\begin{aligned}\ddot{\eta}_2 U_2^T M U_2 + \eta_2 U_2^T K U_2 &= W U_2 - \eta_1 U_1^T K U_2 \\ \Rightarrow \ddot{\eta}_2 M_2 + \eta_2 K_2 &= \tilde{W}\end{aligned}\tag{2.47}$$

where $M_2 = U_2^T M U_2$, $K_2 = U_2^T K U_2$, and $\tilde{W} = W U_2 - \eta_1 U_1^T K U_2$. The second part yields an algebraic equation that is used to solve for the Lagrange Multiplier:

$$\begin{aligned}\ddot{\eta}_2 U_2^T M M^{-1} U_1 + \eta_1 U_1^T K M^{-1} U_1 + \eta_2 U_2^T K M^{-1} U_1 &= W M^{-1} U_1 + \Omega V \Sigma_1^T U_1^T M^{-1} U_1 \\ \Rightarrow N K M^{-1} U_1 - \Omega P^T M^{-1} U_1 &= W M^{-1} U_1\end{aligned}\tag{2.48}$$

Notice that K is also a linear function of Ω from Eqs. (2.41c) and (2.41d), meaning that the matrix of Lagrange multipliers can be obtained analytically by solving the linear algebra problem. The full analytical solution of Ω can be found in Appendix C.

2.7 Dynamics Verification: Double Pendulum

To verify the non-minimal dynamics model developed in the previous section, we will investigate the double pendulum system, which has been well studied in the field of multibody dynamics. As depicted in Figure 2.4, the system comprises two rigid bars with uniform mass distribution. First, we will carry out the analytical solution of the double pendulum by taking the Lagrangian of the system in minimal coordinates. Then, we specify the node and connectivity matrices for the system and numerically implement Eqs. (2.41a-2.41d) to obtain the position history of each node in the structure. By plotting the position errors for each node in the structure, we find that the non-minimal dynamics equations are accurate to machine precision.

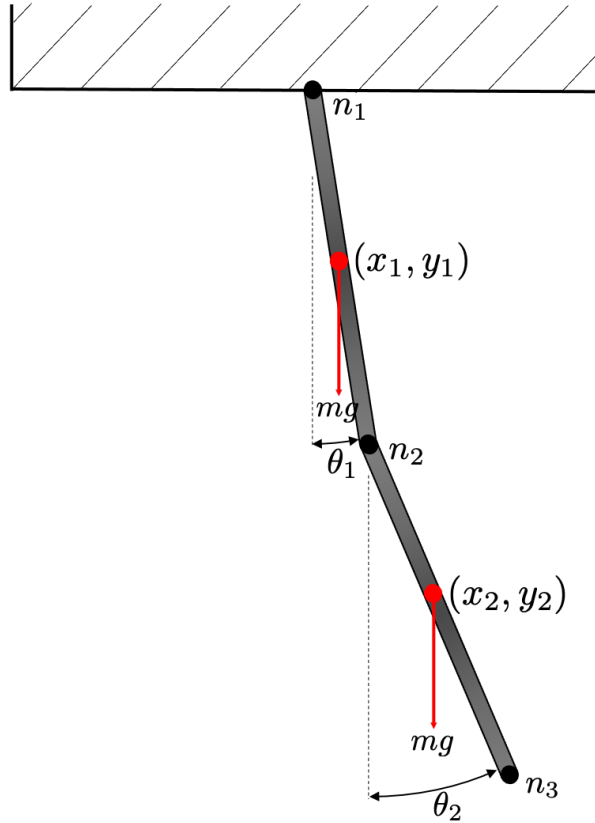


Figure 2.4. Double pendulum system

2.7.1 Analytical Solution

The center of mass of each rigid bar can be located in terms of the minimal coordinates θ_1 and θ_2 as

$$\begin{aligned}
 x_1 &= \frac{\ell}{2} \sin(\theta_1) \\
 y_1 &= -\frac{\ell}{2} \cos(\theta_1) \\
 x_2 &= \ell \left(\sin(\theta_1) + \frac{1}{2} \sin(\theta_2) \right) \\
 y_2 &= -\ell \left(\cos(\theta_1) + \frac{1}{2} \cos(\theta_2) \right)
 \end{aligned}$$

where ℓ is the length of each bar and θ_1 and θ_2 describe the angle of each respective bar from vertical. Define the kinetic energy of the system as

$$T = \frac{m}{2} (\dot{x}_1^2 + \dot{y}_1^2 + \dot{x}_2^2 + \dot{y}_2^2) + \frac{1}{2}I (\dot{\theta}_1^2 + \dot{\theta}_2^2) \quad (2.49)$$

where $I = \frac{1}{12}ml^2$ is the moment of inertia of the bar about its center of mass. The first term in Eq. (2.49) represents the translational kinetic energy of the system while the second term represents the system's rotational kinetic energy. The potential energy of the system is written as

$$V = -mg(y_1 + y_2) \quad (2.50)$$

where y_1 and y_2 represent the vertical height of each respective bar mass center. Now, define the Lagrangian as $\mathcal{L} = T - V$. For a conservative system with no virtual work, Lagrange's Equation can be written in generalized coordinates as

$$\frac{d}{dt} \left(\frac{\partial \mathcal{L}}{\partial \dot{q}} \right) - \frac{\partial \mathcal{L}}{\partial q} = 0 \quad (2.51)$$

where q is the generalized coordinate. In the case of the double pendulum, there are two generalized coordinates (θ_1 and θ_2). Substituting the Lagrangian $\mathcal{L} = T - V$ into Eq. (2.51) and taking the partial derivatives leads to the equations of motion for the double pendulum system:

$$8\ddot{\theta}_1 + 3\ddot{\theta}_2 \cos(\theta_1 - \theta_2) + 3\dot{\theta}_2^2 \sin(\theta_1 - \theta_2) + 9\frac{g}{l} \sin(\theta_1) = 0 \quad (2.52)$$

$$2\ddot{\theta}_2 + 3\ddot{\theta}_1 \cos(\theta_1 - \theta_2) - 3\dot{\theta}_1^2 \sin(\theta_1 - \theta_2) + 3\frac{g}{l} \sin(\theta_2) = 0 \quad (2.53)$$

where we have applied $m_1 = m_2 = 1$ kg, $b_1 = b_2 = \ell = 1$ m.

2.7.2 Numerical Solution

Next, the non-minimal dynamics model is verified by numerically simulating Eqs. (2.41a-2.41d) for the double pendulum system. In the remaining examples, we use a Matlab-based vector dynamics package [38] to integrate the equations of motion with a fourth-order Runge-Kutta integration scheme. For more information on the numerical implementation, see Appendix B for the system dynamics flow charts corresponding to both Class-1 and Class-k tensegrity structures.

To perform a numerical simulation in the tensegrity dynamics package, one must specify the structure's configuration (node and connectivity matrices) as well as the

integration time step and simulation time. In this example, we initialize the double pendulum at an angle of 45 degrees. Following the convention defined above, we prescribe the initial node and connectivity matrices:

$$N_0 = \begin{bmatrix} 0 & \sqrt{2}/2 & \sqrt{2} \\ 0 & -\sqrt{2}/2 & -\sqrt{2} \\ 0 & 0 & 0 \end{bmatrix}, \quad C_b = \begin{bmatrix} -1 & 1 & 0 \\ 0 & -1 & 1 \end{bmatrix}, \quad C_s = \begin{bmatrix} -1 & 1 & 0 \\ 0 & -1 & 1 \end{bmatrix}.$$

By carrying out the multiplication $B = NC_b^T$ and $S = NC_s^T$, one can verify the bar and string vectors in a given tensegrity structure. Due to the nature of the tensegrity software, at least one string must be specified. To account for this, we define massless strings along each bar member. Next, we specify an integration time step of $\Delta t = 0.001$ and numerically integrate the system for a total time of 5 seconds. Figure 2.5(a) depicts the node position histories obtained via the numerical simulation. Next, Eqs. (2.52) and (2.53) are numerically integrated in order to compare the numerical results with the analytically obtained solution.

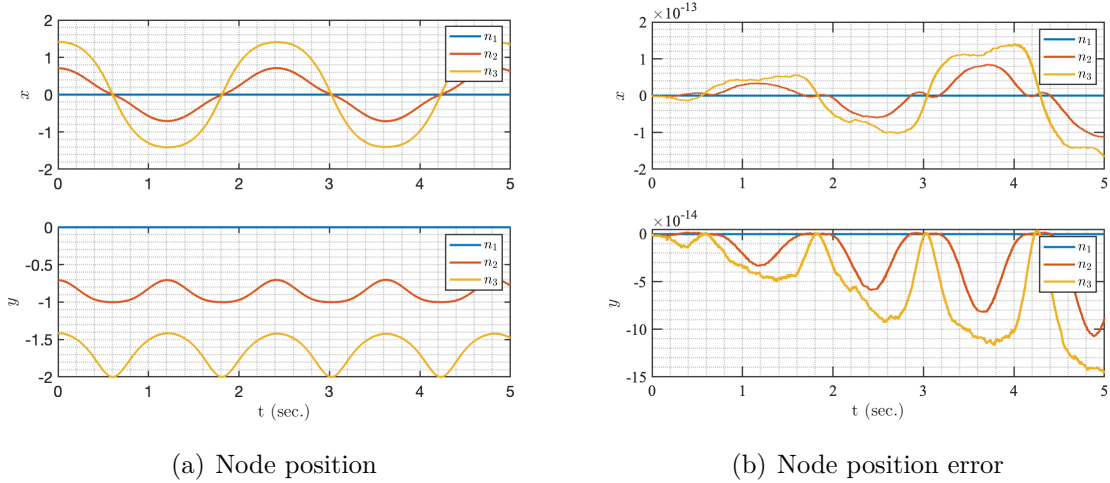


Figure 2.5. Comparison between double pendulum analytical and numerical solution

Figure 2.5(b) depicts the error in node x and y positions between the numerically obtained solution and the analytical solution. We see that the errors are on the order of 10^{-13} and 10^{-14} , which indicates that the simulation results align well with the analytical solution for the double pendulum. This proves that the developed equations of motion for tensegrity system dynamics are sufficiently accurate.

2.8 Class-1 Dynamics Verification: T-bar Simulation

Next, we simulate the open-loop vibrational response of a fundamental tensegrity structure known as the T-bar. The T-bar tensegrity is a 2-dimensional structure that consists of one horizontal bar member and one lateral bar member to form the shape of a cross as depicted in Figure 2.6(a). Four string members are connected around the outer perimeter to prevent global buckling in the structure. Because only one bar resides at any given node, the T-bar is defined as a Class-1 tensegrity structure. Despite its simplicity, the T-bar structure has been shown to exhibit an exceptionally high mass-to-stiffness ratio and is considered to be a minimum mass structure for a given compressive load [39]. The low mass and high stiffness of the T-bar structure makes it an attractive candidate for deployable space structures.

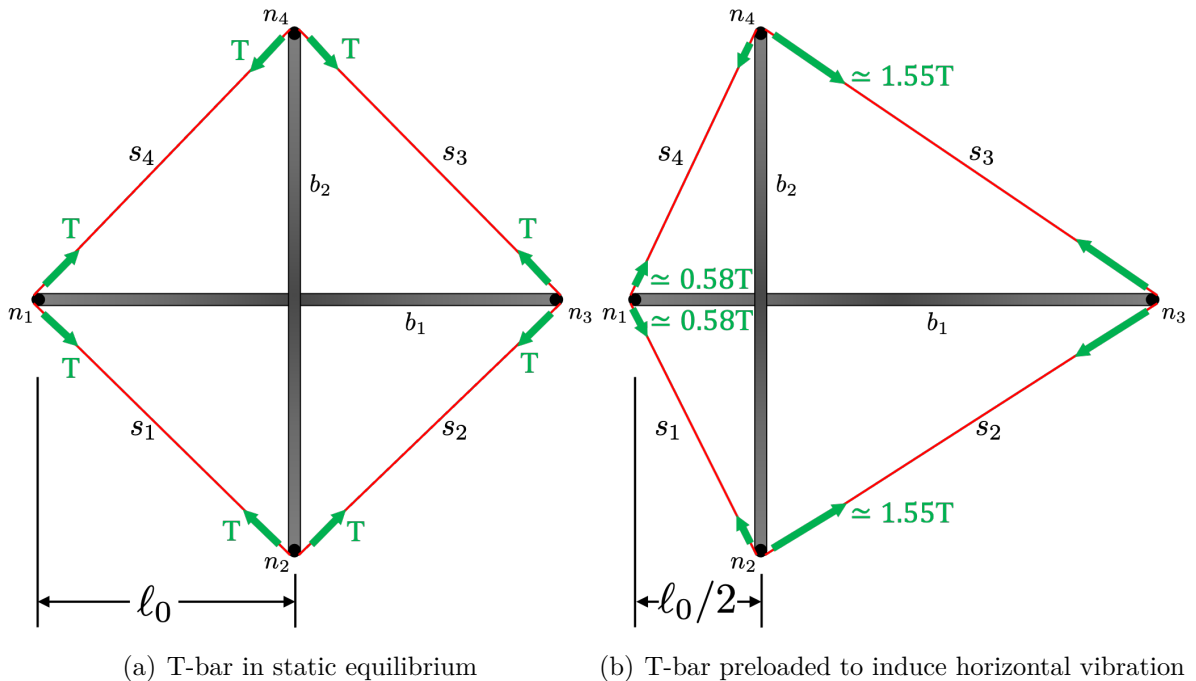


Figure 2.6. T-bar tensegrity system with different initial conditions

In this example, we configure a static T-bar structure with nodes at the locations $(-1, 0)$, $(0, -1)$, $(1, 0)$ and $(0, 1)$. This yields the following node and connectivity matrices:

$$N = \begin{bmatrix} -1 & 0 & 1 & 0 \\ 0 & -1 & 0 & 1 \\ 0 & 0 & 0 & 0 \end{bmatrix}, \quad C_b = \begin{bmatrix} -1 & 0 & 1 & 0 \\ 0 & -1 & 0 & 1 \end{bmatrix}, \quad C_s = \begin{bmatrix} -1 & 1 & 0 & 0 \\ 0 & -1 & 1 & 0 \\ 0 & 0 & -1 & 1 \\ 1 & 0 & 0 & -1 \end{bmatrix}$$

It is convenient to define the distance from the center of the cross to the leftmost node of the equilibrated structure n_1 as ℓ_0 . When the structure is in static equilibrium, each of the strings forms the hypotenuse of an equilateral triangle with length $\|\mathbf{s}_i\| = \sqrt{2}$. We assign pre-stress in the strings by specifying their rest lengths ρ_i (unstretched) to be 50% of their given lengths so that $\rho_i = 0.5 \|\mathbf{s}_i\| = \sqrt{2}/2$. In this example, we prescribe an extensional stiffness of $k = 100$ N/m and no damping ($z = 0$ Ns/m) to each string member. Therefore, the tension in each string of the static T-bar structure can be calculated as $t = t_i = k (\|\mathbf{s}_i\| - \rho_i) = 100 (\sqrt{2} - \sqrt{2}/2)$ N. By observing the free body diagram in Figure 2.6(a), one can easily see how uniform pre-stress in the four strings causes the force balance that is necessary for static equilibrium.

Shifting focus to Figure 2.6(b), we then perturb the structure from its equilibrium by moving the vertical bar member to the left by a distance of $\ell_0/2$. This leads to an uneven distribution of tension in the structure. Using trigonometry, the new tension in strings s_1 and s_4 is calculated as $t_{\text{left}} = 100 (\sqrt{0.5^2 + 1} - \sqrt{2}/2) \approx 0.58t$. Similarly, strings s_2 and s_3 , take on new tension values of $t_{\text{right}} = 100 (\sqrt{1.5^2 + 1} - \sqrt{2}/2) \approx 1.55t$. By looking into the force imbalance depicted in Figure 2.6(b), it is clear to see how asymmetric pre-stress will induce vibration in the T-bar structure.

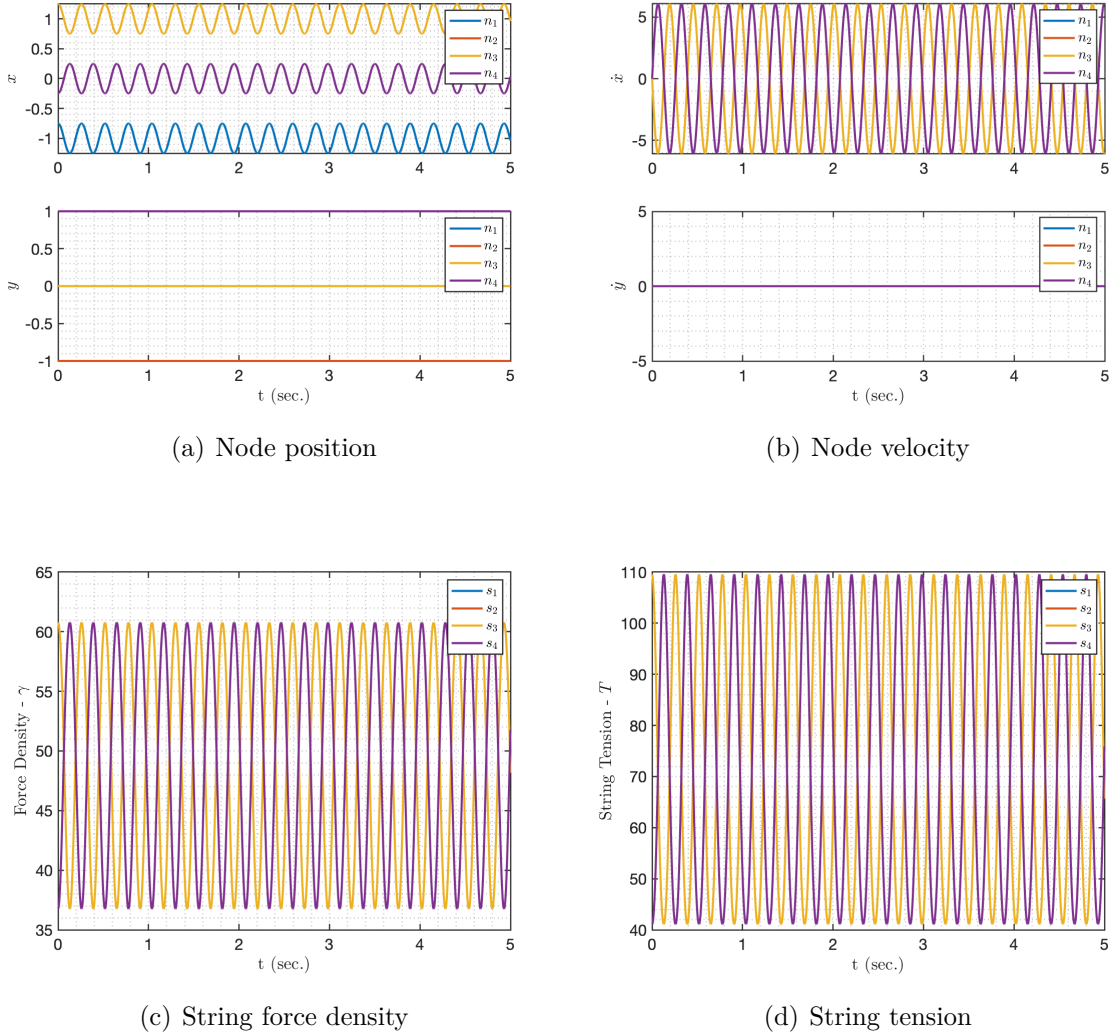


Figure 2.7. Initial condition response of the horizontally preloaded T-bar system

To collect free response data for the T-bar, we initialize the structure in the preloaded state of Figure 2.6(b) and simulate for a total time of 5 seconds with an integration time step of $\Delta t = 0.001$ seconds. Figure 2.9(a) depicts the position of each node over the 5 second interval. As expected, the y -positions of the four nodes do not change over the time interval. The x -position of each node oscillates about the static equilibrium condition at a frequency of roughly 3.73 Hz. If there were damping in the strings ($z \neq 0$), then the structure would eventually return to its static equilibrium position. In Figure 2.9(c), we see that the force density in the strings oscillates between roughly 36 N/m and 61 N/m. The string tensions, depicted in Figure 2.9(d), are obtained by multiplying the force densities by the corresponding string lengths at each time step.

2.9 Class-k Dynamics Verification: D-bar Simulation

In this section, we investigate the free response of another fundamental tensegrity structure known as the D-bar. Depicted in Figure 2.8(a), the D-bar tensegrity structure comprises two tensile members and four compressive members arranged in the shape of a diamond. At each node, two bar members are connected through frictionless ball joints [3], making the D-bar a Class-2 tensegrity structure. The vertical string supports a compressive load applied at the two end points while the horizontal string is needed to stabilize the structure and maintain static equilibrium. As we will see later, the horizontal string can also be utilized to deploy the structure. The D-bar is regarded as a minimum mass structure for a given tensile load. It is also considered to be the topological dual of the T-bar structure, as the two structures exchange compressive members for tensile members [39]. Because the tendons have the ability to articulate each Class-2 joint, the D-bar has the unique feature of being deployable and presents a high packaging efficiency. These characteristics makes the D-bar a suitable candidate for deployable, articulated space structures.

We configure a static D-bar structure with nodes at the locations $(-1, 0)$, $(0, -1)$, $(1, 0)$ and $(0, 1)$. This yields the following node and connectivity matrices:

$$N = \begin{bmatrix} -1 & 0 & 1 & 0 \\ 0 & -1 & 0 & 1 \\ 0 & 0 & 0 & 0 \end{bmatrix}, \quad C_b = \begin{bmatrix} 1 & 0 & 0 & -1 \\ -1 & 1 & 0 & 0 \\ 0 & -1 & 1 & 0 \\ 0 & 0 & -1 & 1 \end{bmatrix}, \quad C_s = \begin{bmatrix} 0 & -1 & 0 & 1 \\ -1 & 0 & 1 & 0 \end{bmatrix}$$

In this configuration, the strings have length $\|\mathbf{s}_i\| = 2$. We prescribe pre-stress in the strings by setting their rest lengths to 50% of the given lengths, so that $\rho_i = 1$. Assigning stiffness $k = 100$ N/m and damping $z = 0$ Ns/m to each string member yields a tension of $t = k(\|\mathbf{s}_i\| - \rho_i) = 100(2 - 1) = 100$ N in each static string member. Looking into the free body diagram depicted in Figure 2.8(a), one can easily see how uniform tension keeps the D-bar structure in static equilibrium.

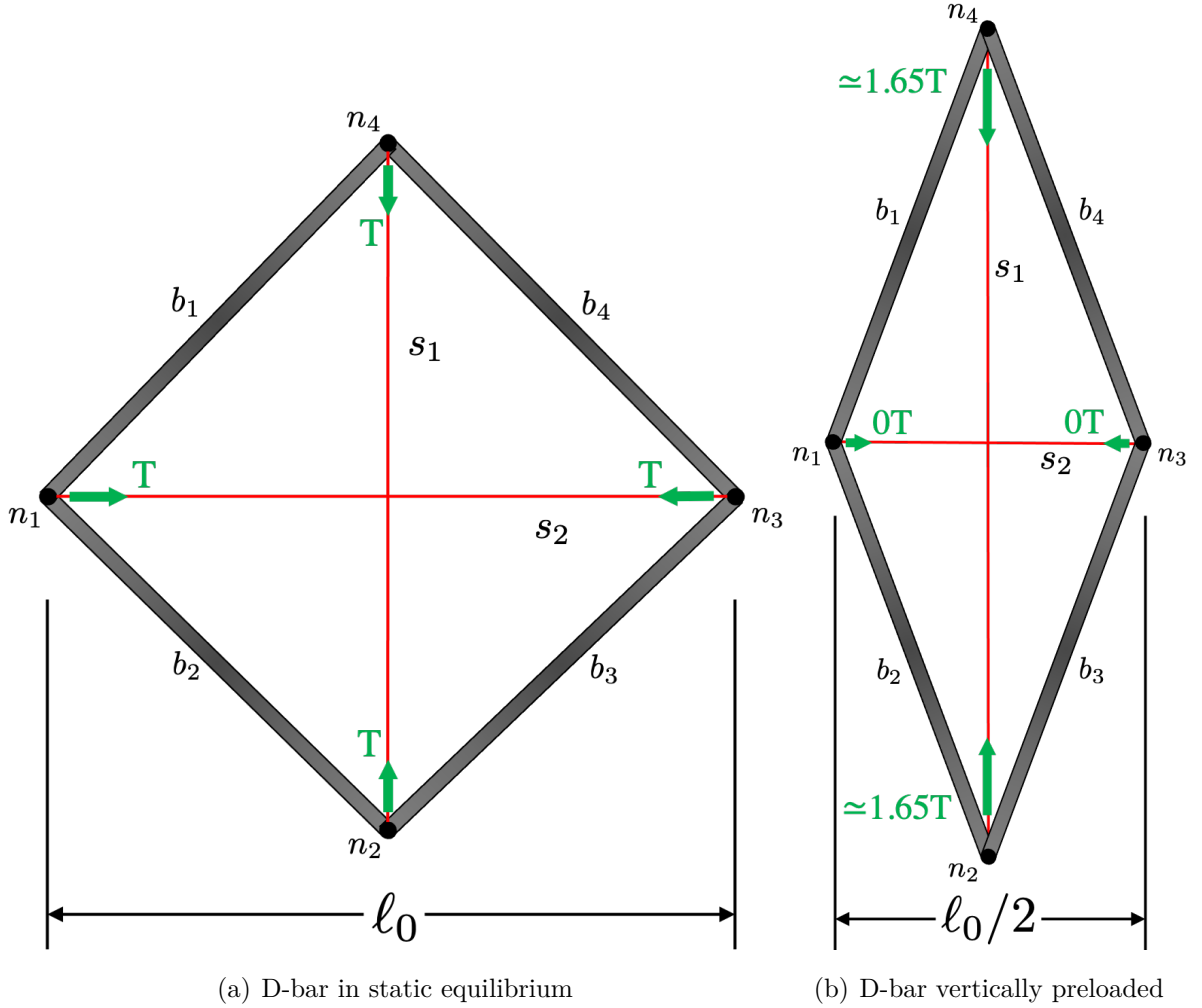


Figure 2.8. D-bar tensegrity system with different initial conditions

Now, shifting our attention to Figure 2.8(b), we perturb the D-bar structure from its static equilibrium by halving the distance between node n_1 and node n_3 . At this point, the given length of string s_2 is equal to its rest length, ρ_2 . Therefore, there is no initial pre-stress in string s_2 of the perturbed D-bar structure in Figure 2.8(b). On the other hand, the tension in string s_1 increases to $t_1 = 100 \left(2\sqrt{2} - 0.5^2 - 1 \right) \approx 1.65t$. Due to the force imbalance between strings, the perturbed D-bar is set into motion.

In this example, the D-bar is initialized in the preloaded state of Figure 2.8(b) to induce motion. Using the class-k equations of motion, we simulate the D-bar structure for a total time of 5 seconds with an integration time step of $\Delta t = 0.001$ seconds. Figure 2.9 depicts the free response data for the D-bar structure. Looking into Figure 2.9(a), we see that the D-bar structure oscillates about its static equilibrium position at a frequency of approximately 1.87 Hz after being perturbed. The D-bar's frequency of oscillation is

approximately half that of the T-bar, likely due to the added mass of the two additional bar members. Moreover, we see in Figure 2.9(c) that the force density of the structure oscillates between roughly 62 N/m and 0 N/m. In the next chapter, we'll design a shape control law to regulate the force density in each string based on desired control objectives.

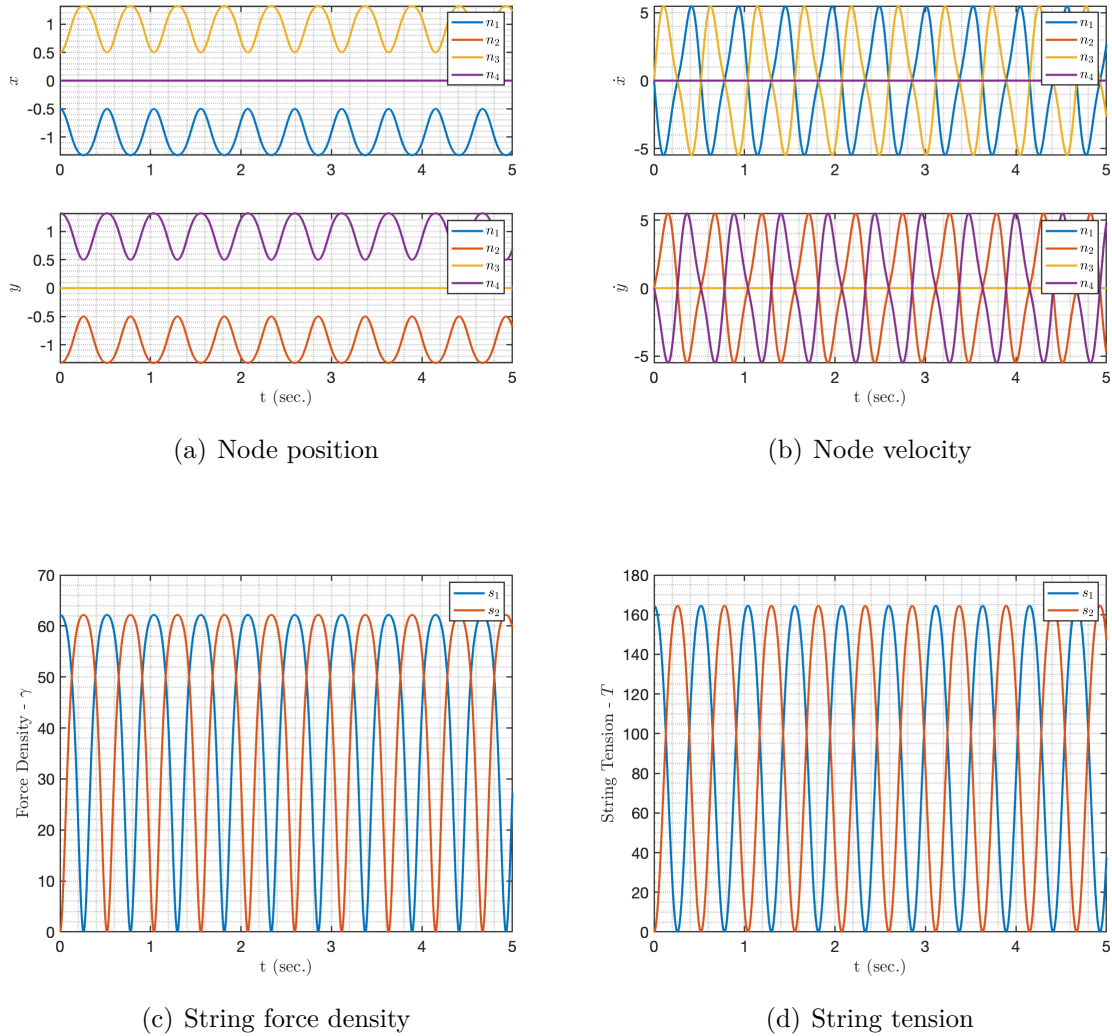


Figure 2.9. Initial condition response of the vertically preloaded D-bar system

Chapter 3 |

Model-based Shape Control

In the previous chapter, we developed the equations of motion to simulate tensegrity systems in a non-minimal coordinate system. This enabled the system dynamics to be written compactly in the matrix form. In this chapter, we will utilize our dynamics model to derive a model-based feedback control law to control the shape of a tensegrity structure. Our approach builds upon recent contributions made by Skelton and Henrickson [40]. In this approach, we define the control variable as the string force density vector so that the system dynamics can be written linearly in terms of the control variable. This allows us to solve for the control at each time step with linear programming. The physical control variable (string tensions) can be easily obtained by multiplying the string force density vector by the vector of string lengths at each time step.

We begin this chapter by defining shape objectives to regulate particular nodes in the structure and then utilize Lyapunov theory to assess the stability of tendon-actuated tensegrity systems. Next, we derive a state-feedback control law to solve for the control signal which regulates node positions to a specified reference trajectory. After developing the shape control law, we return our attention to the T-bar and D-bar tensegrity structures, this time implementing the control law to maneuver between desired shapes in simulation. Finally, we demonstrate the performance of the developed controller by controlling the T-bar and D-bar tensegrity structures through a wide range of shapes.

3.1 State Feedback

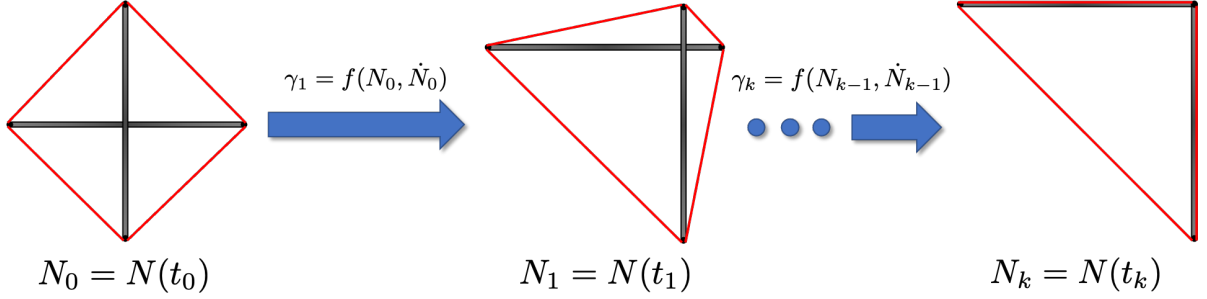


Figure 3.1. Quasi-static shape change

Recall that Eqs. (2.41a)-(2.41d) govern the full nonlinear motion of Class-k tensegrity systems. In this work, we define the control variable as the string force density vector, $\boldsymbol{\gamma} \in \mathbb{R}^{\alpha \times 1}$, where α is the number of strings in the structure. This means that tensegrity system dynamics are linear in the control but nonlinear with respect to the state. We can write Eq. (2.41a) in a general nonlinear form as

$$\dot{\boldsymbol{x}} = f(\boldsymbol{x}) + g(\boldsymbol{x})\boldsymbol{u} \rightarrow \ddot{N} = f(N, \dot{N}) + g(N)(\hat{\boldsymbol{\gamma}})h(N, \dot{N}). \quad (3.1)$$

Systems in the form of Eq. (3.1) are known as *control-affine systems* or *affine-in-control systems* and have been studied extensively in nonlinear control theory [41, 42]. A state feedback control law (i.e., closed-loop) is developed to regulate the tensegrity structure between different equilibrium configurations. A feedback controller is desirable due to their insensitivity to state perturbations and external disturbance while guaranteeing stability [43]. The primary objective of this chapter is to utilize our dynamics model to design a control law that will move the tensegrity structure between its static equilibria.

In the previous chapter, we studied the free response of the T-bar tensegrity structure about its symmetric equilibrium position. As we will see next, the T-bar is considered to be in static equilibrium as long as the two bar members are overlapping, as in Figure 3.1. When the bar members overlap, string tensions can be found to sufficiently equilibrate the structure through force balance. In general, a tensegrity system is in static equilibrium when the node vectors are inertially fixed. Substituting $\dot{N} = 0$ and $\ddot{N} = 0$ into Eq. (2.41a), we have the static equilibrium condition:

$$NK = N \left(C_s^T \hat{\boldsymbol{\gamma}} C_s - C_b^T \hat{\boldsymbol{\lambda}} C_b \right) = W + \Omega P^T, \quad (3.2)$$

The set of node matrices satisfying Eq. (3.2) for given a connectivity (C_b and C_s) constitute the geometric solution space for a given tensegrity structure. This process of finding the whole range of equilibrated shapes for a given tensegrity structure continues to be a growing area of research [18]. In this work, we focus on developing a control law that can be used to dynamically maneuver between static equilibria in the geometric solution space of any tensegrity structure. That is, given an initial shape and a desired final shape, we derive a control policy to dynamically regulate the structure between these two states (the intermediate steps in Figure 3.1). We call this type of motion ‘quasi-static’.

3.2 Shape Objectives

To maintain flexibility in the control law, we define two matrices, $L \in \mathbb{R}^{j \times 3}$ and $R \in \mathbb{R}^{n \times h}$, that specify which axes and nodes are to be controlled, where j is the number of “axes of interest” and h is the number of “nodes of interest”. By multiplying $LN R$, we identify the “node coordinates of interest”. The goal is to regulate the node coordinates of interest to some desired final shape or trajectory. Therefore, we must also define $\bar{Y} \in \mathbb{R}^{j \times h}$, whose columns are the corresponding node coordinates of the desired final shape. One can similarly define a reference trajectory by specifying \bar{Y} as a function of time. The reference trajectory can be user provided or can be the outcome of an optimal trajectory generation process. The node position error and its time derivatives are written as

$$E = LN R - \bar{Y} = L(\eta_1 U_1^T + \eta_2 U_2^T)R - \bar{Y} \quad , \quad \dot{E} = L\dot{\eta}_2 U_2^T R \quad , \quad \ddot{E} = L\ddot{\eta}_2 U_2^T R. \quad (3.3)$$

where we recall that $\dot{\eta}_1 = 0$ and $\ddot{\eta}_1 = 0$ due to the no-motion space.

3.3 Stability Considerations

To begin, we define the candidate Lyapunov Function $V(N, \dot{N})$:

$$V(N, \dot{N}) = \frac{1}{2} \text{Tr}(E^T \Theta E + \dot{E}^T \dot{E}) > 0 \quad \forall [E, \dot{E}] \neq 0 \quad (3.4)$$

where $\text{Tr}(\circ)$ is the trace operator and the matrix $\Theta > 0$ (positive definite), allows us to change the weights between position error and position error velocity. The first time derivative of Eq. (3.4) is

$$\dot{V} = \text{Tr}(\dot{E}^T \Theta E + \dot{E}^T \ddot{E}). \quad (3.5)$$

For asymptotic stability, we require the time derivative of the candidate Lyapunov function to be negative definite, i.e.,

$$\dot{V} = -\text{Tr}(\dot{E}^T \Psi \dot{E}) < 0 \quad (3.6)$$

where Ψ is any positive definite matrix. Substituting Eq. (3.6) into Eq. (3.5), we obtain

$$\text{Tr}(\dot{E}^T \ddot{E} + \dot{E}^T \Psi \dot{E} + \dot{E}^T \Theta E) = 0. \quad (3.7)$$

After using the properties of the trace operator, we obtain the following expression for the closed loop error dynamics:

$$\ddot{E} + \dot{E}\Psi + E\Theta = 0. \quad (3.8)$$

Note that the closed-loop error dynamics follow a second order spring mass damper structure with the matrix Ψ being the equivalent damping and the matrix Θ being the equivalent stiffness.

3.4 Position Control

Eq. (3.8) is a second-order differential equation in the error dynamics which is used to regulate node coordinates by tuning the control gain matrices, $\Psi \in \mathbb{R}^{h \times h}$ and $\Theta \in \mathbb{R}^{h \times h}$ for the desired performance. To begin, formulating the control law as a linear algebra problem requires writing the bar force density vector as a linear function of the string force density vector. This is done by first writing the i^{th} diagonal element of Eq. (2.41d) as

$$\lambda_i = -J_i l_i^{-2} \mathbf{e}_i^T \left[\dot{B}^T \dot{B} \right] \mathbf{e}_i - \frac{1}{2} l_i^{-2} \mathbf{e}_i^T \left[B^T (W + \Omega P^T - S \hat{\gamma} C_s) C_b^T \right] \mathbf{e}_i \quad (3.9)$$

where \mathbf{e}_i is a column vector of zeros except for the i^{th} element, which is equal to one. To isolate γ , we utilize the algebraic manipulation $\hat{x}y = \hat{y}x$ where x and y are both column vectors. Recall that the $\{\hat{\cdot}\}$ operator forms a diagonal matrix from the elements of a vector. Applying this to Eq. (3.9) and stacking each i^{th} diagonal element into a column vector:

$$\boldsymbol{\lambda} = \Lambda \boldsymbol{\gamma} + \boldsymbol{\tau} \quad (3.10)$$

where

$$\begin{aligned} \Lambda &= \left[\Lambda_1^T \ \Lambda_2^T \ \cdots \ \Lambda_\beta^T \right]^T, \quad \boldsymbol{\tau} = \left[\tau_1^T \ \tau_2^T \ \cdots \ \tau_\beta^T \right]^T, \\ \tau_i &= -J_i l_i^{-2} \|\dot{b}_i\|^2 - \frac{1}{2} l_i^{-2} b_i^T (W + \Omega P^T) C_b^T \mathbf{e}_i, \\ \Lambda_i &= \frac{1}{2} l_i^{-2} b_i^T S(\widehat{C_s C_b^T \mathbf{e}_i}) \quad \text{for } i = 1, 2 \cdots \beta. \end{aligned}$$

Returning our attention to the error dynamics, we substitute Eq. (2.47) and Eq. (3.3) into Eq. (3.8) to obtain

$$\begin{aligned} L(WU_2 - \eta_1 U_1^T K U_2 - \eta_2 U_2^T K U_2) M_2^{-1} U_2^T R + L \dot{\eta}_2 U_2^T R \Psi \\ + \left[L(\eta_1 U_1^T + \eta_2 U_2^T) R - \bar{Y} \right] \Theta = 0. \end{aligned} \quad (3.11)$$

Rearranging Eq. (3.11) to isolate known terms,

$$\begin{aligned} L W U_2 M_2^{-1} U_2^T R + L \dot{\eta}_2 U_2^T R \Psi + \left[L(\eta_1 U_1^T + \eta_2 U_2^T) R - \bar{Y} \right] \Theta \\ = L(\eta_1 U_1^T K U_2 + \eta_2 U_2^T K U_2) M_2^{-1} U_2^T R, \end{aligned} \quad (3.12)$$

where we can simplify the right hand of Eq. (3.12) as

$$L(\eta_1 U_1^T K U_2 + \eta_2 U_2^T K U_2) M_2^{-1} U_2^T R = L N K U_2 M_2^{-1} U_2^T R \quad (3.13)$$

Substituting Eq. (2.41c) into the righthand side of Eq. (3.13) and taking the i^{th} column yields

$$L N K U_2 M_2^{-1} U_2^T R \mathbf{e}_i = L N C_s^T \hat{\boldsymbol{\gamma}} C_s U_2 M_2^{-1} U_2^T R \mathbf{e}_i - L N C_b^T \hat{\boldsymbol{\lambda}} C_b U_2 M_2^{-1} U_2^T R \mathbf{e}_i. \quad (3.14)$$

Applying the algebraic manipulation $\hat{\boldsymbol{x}} \mathbf{y} = \hat{\mathbf{y}} \boldsymbol{x}$ to the righthand side of Eq. (3.14) yields

$$L N K U_2 M_2^{-1} U_2^T R \mathbf{e}_i = L N C_s^T (\widehat{C_s U_2 M_2^{-1} U_2^T R \mathbf{e}_i}) \boldsymbol{\gamma} - L N C_b^T (\widehat{C_b U_2 M_2^{-1} U_2^T R \mathbf{e}_i}) \boldsymbol{\lambda}. \quad (3.15)$$

Now, substituting Eq. (3.10) into Eq. (3.15) yields

$$\begin{aligned} LNKU_2M_2^{-1}U_2^TRe_i &= -LNC_b^T(\overline{C_bU_2M_2^{-1}U_2^TRe_i})\boldsymbol{\tau} \\ &+ \left(LNC_s^T(\overline{C_sU_2M_2^{-1}U_2^TRe_i}) - LNC_b^T(\overline{C_bU_2M_2^{-1}U_2^TRe_i})\Lambda \right)\boldsymbol{\gamma}. \end{aligned} \quad (3.16)$$

Finally, substituting Eq. (3.16) back into Eq. (3.12) and repeating this process for every column yields a linear algebra problem that is used to solve for the string force density vector at each time step:

$$\begin{bmatrix} \Gamma_1 \\ \Gamma_2 \\ \vdots \\ \Gamma_h \end{bmatrix} \begin{Bmatrix} \gamma_1 \\ \gamma_2 \\ \vdots \\ \gamma_\alpha \end{Bmatrix} = \begin{bmatrix} \boldsymbol{\mu}_1 \\ \boldsymbol{\mu}_2 \\ \vdots \\ \boldsymbol{\mu}_h \end{bmatrix} \quad (3.17)$$

where

$$\begin{aligned} \Gamma_i &= LNC_s^T(\overline{C_sU_2M_2^{-1}U_2^TRe_i}) - LNC_b^T(\overline{C_bU_2M_2^{-1}U_2^TRe_i})\Lambda \\ \boldsymbol{\mu}_i &= \left(LWU_2M_2^{-1}U_2^TR + L\dot{\eta}_2U_2^TR\Psi + [L(\eta_1U_1^T + \eta_2U_2^T)R - \bar{Y}] \Theta \right) \mathbf{e}_i \\ &+ LNC_b^T(\overline{C_bU_2M_2^{-1}U_2^TRe_i})\boldsymbol{\tau} \end{aligned}$$

$$\text{for } i = 1, 2 \dots h$$

and h is the number of nodes of interest. Here, we have the dimensions $\boldsymbol{\gamma} \in \mathbb{R}^{\alpha \times 1}$, $\Gamma \in \mathbb{R}^{jh \times \alpha}$, and $\boldsymbol{\mu} \in \mathbb{R}^{jh \times 1}$. Because the tensegrity structure is generally an underactuated system (less strings than degrees of freedom), one must carefully choose the node coordinates of interest so that Eq. (3.17) becomes an underdetermined system. In the overdetermined case ($jh > \alpha$), one cannot guarantee a solution for the control variable. Physically, this translates to assuring that there are enough strings in the structure to regulate the node coordinates of interest.

3.5 Velocity and Acceleration Control

In the previous section, we showed how to regulate the node positions in a tensegrity structure by defining the node position error $E_p = L_pNR_p - \bar{Y}_p$. Here, we introduce the

subscript to emphasize that the error corresponds to node positions only. In this section, we'll detail a similar process to control the velocity and acceleration of certain nodes in the structure. To begin, Eq. (3.17) can be written compactly as

$$\Gamma_p \boldsymbol{\gamma} = \boldsymbol{\mu}_p, \quad \boldsymbol{\gamma} > 0. \quad (3.18)$$

To control the velocity of nodes in the structure, we define the node velocity error

$$E_v = L_v \dot{N} R_v - \dot{Y}_v \quad (3.19)$$

and we use a first order equation in the velocity error dynamics:

$$\dot{E}_v + E_v \Psi_v = 0. \quad (3.20)$$

In this case, only the first derivative of error E_v is needed to regulate the node velocity. Now, taking the same approach as discussed in Section 3.4, we arrive at a linear algebra problem used to solve for the string force densities which regulate the node velocity error:

$$\begin{bmatrix} \Gamma_{v_1} \\ \Gamma_{v_2} \\ \vdots \\ \Gamma_{v_h} \end{bmatrix} \begin{Bmatrix} \gamma_1 \\ \gamma_2 \\ \vdots \\ \gamma_\alpha \end{Bmatrix} = \begin{bmatrix} \boldsymbol{\mu}_{v_1} \\ \boldsymbol{\mu}_{v_2} \\ \vdots \\ \boldsymbol{\mu}_{v_h} \end{bmatrix} \quad (3.21)$$

where

$$\begin{aligned} \Gamma_{v_i} &= L_v N C_s^T \overbrace{(C_s U_2 M_2^{-1} U_2^T R_v \mathbf{e}_i)} - L_v N C_b^T \overbrace{(C_b U_2 M_2^{-1} U_2^T R_v \mathbf{e}_i)} \Lambda \\ \boldsymbol{\mu}_{v_i} &= \left(L_v W U_2 M_2^{-1} U_2^T R_v + \left(L_v \dot{\eta}_2 U_2^T R_v - \dot{Y}_v \right) \Psi_v \right) \mathbf{e}_i \\ &\quad + L_v N C_b^T \overbrace{(C_b U_2 M_2^{-1} U_2^T R_v \mathbf{e}_i)} \boldsymbol{\tau} \end{aligned}$$

$$\text{for } i = 1, 2 \dots h$$

We can write Eq. (3.21) compactly as

$$\Gamma_v \boldsymbol{\gamma} = \boldsymbol{\mu}_v, \quad \boldsymbol{\gamma} > 0. \quad (3.22)$$

Now, the node acceleration error can be written as

$$E_a = L_a \ddot{N} R_a - \ddot{Y}_a. \quad (3.23)$$

The error dynamics can be achieved directly by setting Eq. (3.23) to zero as

$$E_a = 0. \quad (3.24)$$

Again, using the same procedure as discussed in the previous section, we arrive at a linear algebra problem used to solve for the string force densities which regulate the node acceleration error:

$$\begin{bmatrix} \Gamma_{a_1} \\ \Gamma_{a_2} \\ \vdots \\ \Gamma_{a_h} \end{bmatrix} \begin{Bmatrix} \gamma_1 \\ \gamma_2 \\ \vdots \\ \gamma_\alpha \end{Bmatrix} = \begin{bmatrix} \boldsymbol{\mu}_{a_1} \\ \boldsymbol{\mu}_{a_2} \\ \vdots \\ \boldsymbol{\mu}_{a_h} \end{bmatrix} \quad (3.25)$$

where

$$\begin{aligned} \Gamma_{a_i} &= L_a N C_s^T \overbrace{(C_s U_2 M_2^{-1} U_2^T R_a \mathbf{e}_i)} - L_a N C_b^T \overbrace{(C_b U_2 M_2^{-1} U_2^T R_a \mathbf{e}_i)} \Lambda \\ \boldsymbol{\mu}_{a_i} &= \left(L_a W U_2 M_2^{-1} U_2^T R_a - \ddot{Y}_a \right) \mathbf{e}_i + L_a N C_b^T \overbrace{(C_b U_2 M_2^{-1} U_2^T R_a \mathbf{e}_i)} \boldsymbol{\tau} \end{aligned}$$

for $i = 1, 2 \dots h$

which can be written compactly as

$$\Gamma_a \boldsymbol{\gamma} = \boldsymbol{\mu}_a, \quad \boldsymbol{\gamma} > 0. \quad (3.26)$$

Finally, combining Eqs. (3.18), (3.22) and (3.26) into a single linear algebra problem allows us to simultaneously control the position, velocity and acceleration of the desired node coordinates as

$$\begin{bmatrix} \Gamma_p \\ \Gamma_v \\ \Gamma_a \end{bmatrix} \boldsymbol{\gamma} = \begin{bmatrix} \boldsymbol{\mu}_p \\ \boldsymbol{\mu}_v \\ \boldsymbol{\mu}_a \end{bmatrix}, \quad \boldsymbol{\gamma} > 0. \quad (3.27)$$

3.6 Control Law Implementation

It is very important to consider that the strings cannot physically provide a compressive force and therefore must always remain in tension to prevent slackness. Mathematically, this can be accounted for by augmenting Eq. (3.27) with the positive string force density

constraint ($\gamma > 0$). In numerical simulations, we obtain the control signal by solving the convex optimization problem:

$$\begin{aligned} & \text{minimize:} && \|\gamma\|_2 \\ & \text{subject to:} && \Gamma\gamma = \boldsymbol{\mu}, \gamma > 0. \end{aligned} \tag{3.28}$$

To solve Eq. (3.28), we use CVX, a package for specifying and solving convex programs [44], [45].

3.7 Case Study: T-bar Position Control

To verify the newly developed shape control law, we return our attention to the T-bar tensegrity structure, a standard baseline for testing in two dimensions. Our new objective is to move the T-bar from the initial shape depicted in Figure 3.2(a) to the final shape of Figure 3.2(d). In this example and the following examples, bar elements are depicted in black while string elements are depicted in red. Specifically, we aim to move nodes n_1 and n_2 to the coordinate position $(0.5, 0.5)$. To proceed in this effort, we must specify the control objective matrices L , R and \bar{Y} as well as the control gain matrices Ψ and Θ . The control objective matrices are as follows:

$$L = \begin{bmatrix} 1 & 0 & 0 \\ 0 & 1 & 0 \end{bmatrix}, \quad R = \begin{bmatrix} 1 & 0 \\ 0 & 1 \\ 0 & 0 \\ 0 & 0 \end{bmatrix}, \quad \bar{Y} = \begin{bmatrix} 0.5 & 0.5 \\ 0.5 & 0.5 \end{bmatrix}.$$

Recall that the dimension of control objective matrices governs the overall dimension of the linear algebra problem. In order to guarantee solutions to Eq. (3.28), the control designer should specify a total number of control objectives that is less than or equal to the total number of strings in the structure. In this case, we have specified $L \in \mathbb{R}^{2 \times 3}$ and $R \in \mathbb{R}^{4 \times 2}$ so that $\Gamma \in \mathbb{R}^{4 \times 4}$ and therefore the system in Eq. (3.28) is uniquely determined. For this particular example, the control gain matrices are

$$\Psi = \begin{bmatrix} 3 & 0 \\ 0 & 3 \end{bmatrix}, \quad \Theta = \begin{bmatrix} 1 & 0 \\ 0 & 1 \end{bmatrix}.$$

Recall that the control gain matrices Ψ and Θ must be positive definite for asymptotic stability. In a standard test case, it is common to start by making the control gain

matrices equal to the identity matrix of equal dimension. However, in this case we have increased the derivative gain matrix Ψ to $3I$ due to stability issues that resulted in excessive overshoot. Increasing the derivative gain matrix Ψ has the effect of decreasing the overshoot while slowing down the rise time. On the other hand, increasing the proportional gain matrix Θ has the effect of decreasing the rise time but increases the overshoot. For all of the remaining examples, the string material parameters are set to $k = 100$ and $z = 0$. The integration time step is $\Delta t = 0.01$ and we simulate the maneuver for a total time of 10 seconds. A four image time lapse is provided in Figure 3.2.

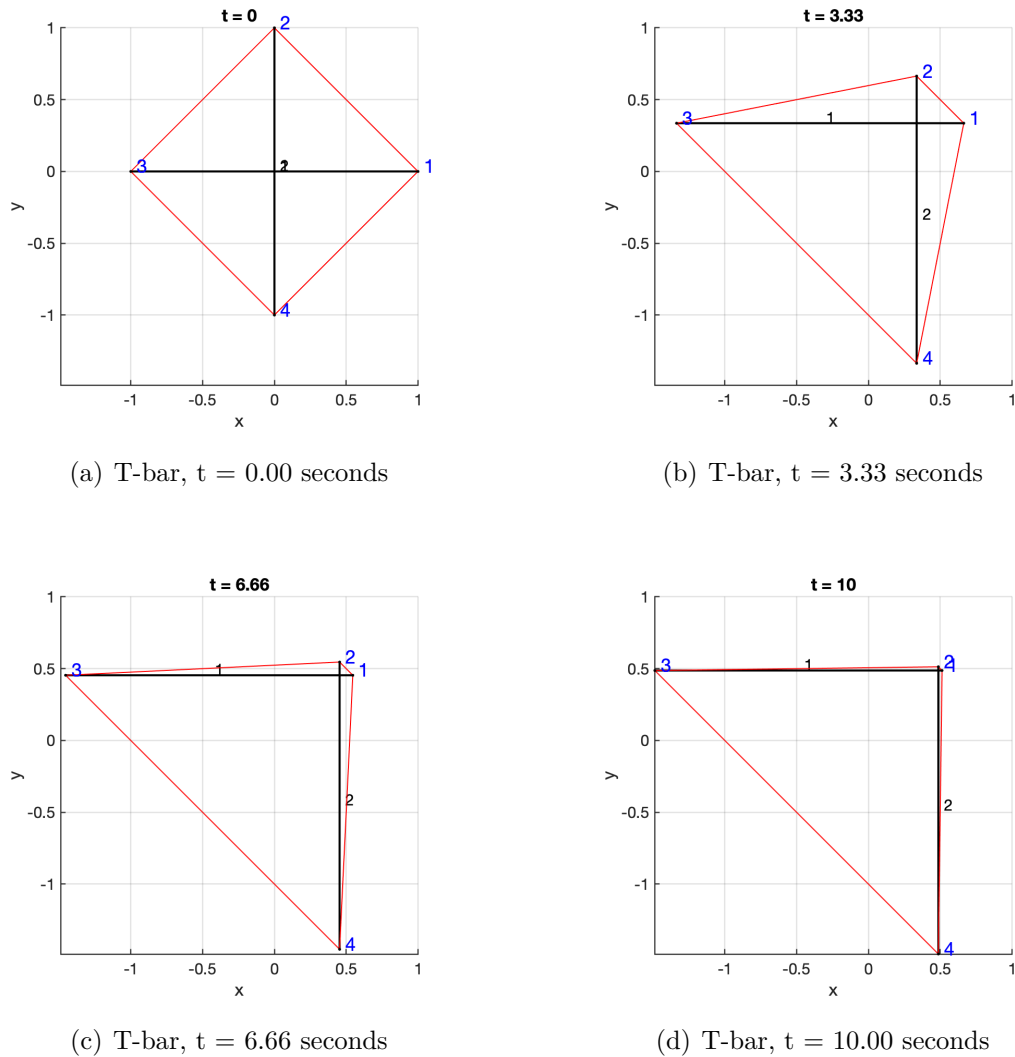


Figure 3.2. T-bar position control sequence

By observing Figure 3.2, we can immediately see that the position controller succeeded in driving nodes n_1 and n_2 to the desired final location of $(0.5, 0.5)$. To gain further

insight into the controller’s performance, the node position history, node velocity history and string force density are depicted in Figure 3.3.

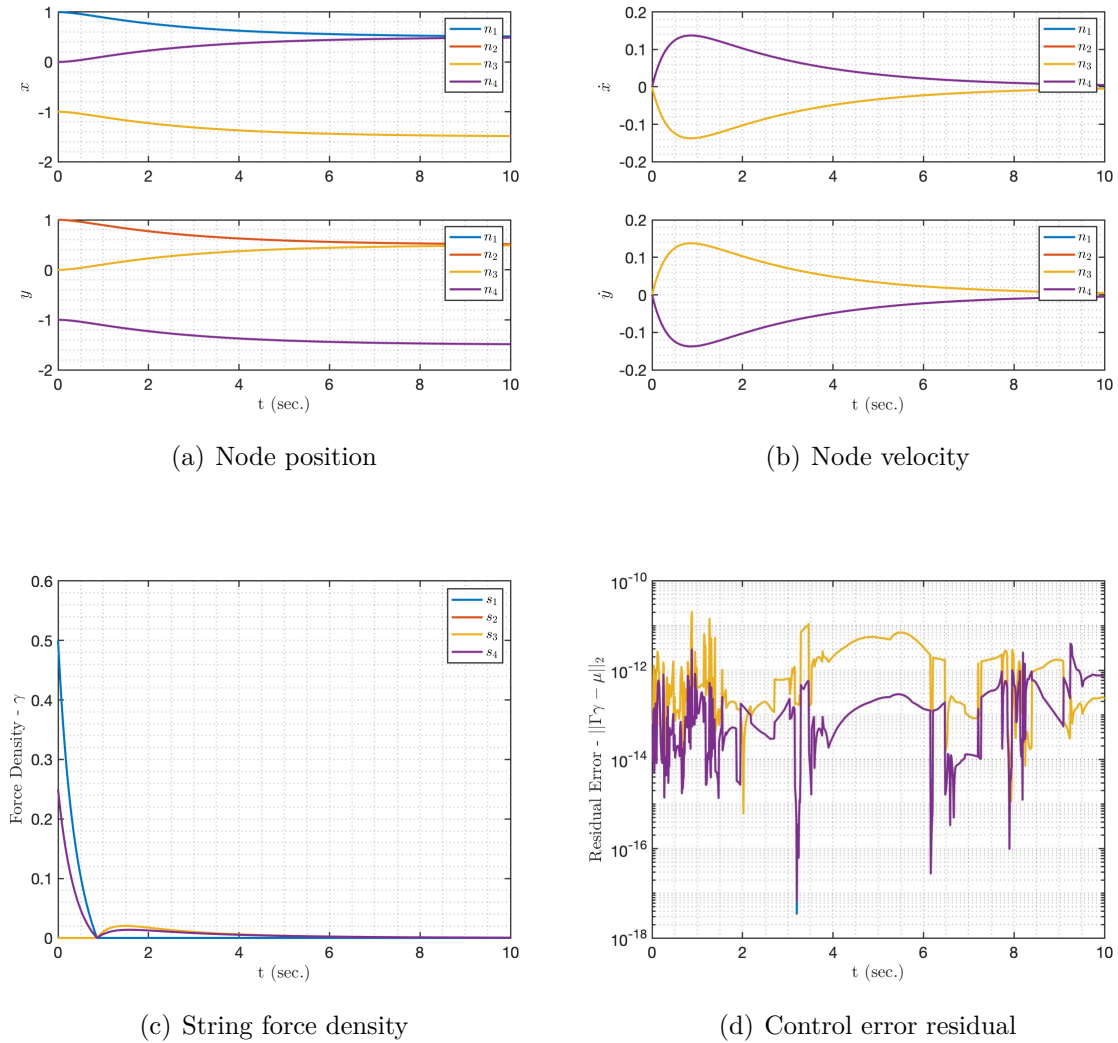


Figure 3.3. T-bar position control simulation results

Within 8 seconds, nodes n_1 and n_2 are already within 0.05 m of the desired location. At this point, the node velocity is nearly zero, which indicates that increasing Ψ did have the effect of reducing the overshoot. The string force density history, depicted in Figure 3.3(c), varies between 0 and 0.5 N/m. At the beginning of the maneuver, strings s_1 and s_4 located on the right hand side of the structure have the highest string force density. This has the desired effect of pulling nodes n_1 and n_2 towards the desired location. At time $t = 1$ sec., strings s_3 and s_4 are engaged to minimize overshoot. In Figure 3.3(d), the residual error $\|\Gamma\gamma - \mu\|_2$ is plotted on a log scale. We see that the controller was

able to find feasible solutions roughly on the order of 10^{-14} , which is within machine precision.

3.8 Case Study: D-bar Position Control

In this example, we turn our attention back to the D-bar tensegrity structure. The objective here is to move the structure from the initial shape depicted in Figure 3.5(a) to the desired shape of Figure 3.5(d). More specifically, our goal here is to move node n_3 to the position $(0.5, 0.5)$.

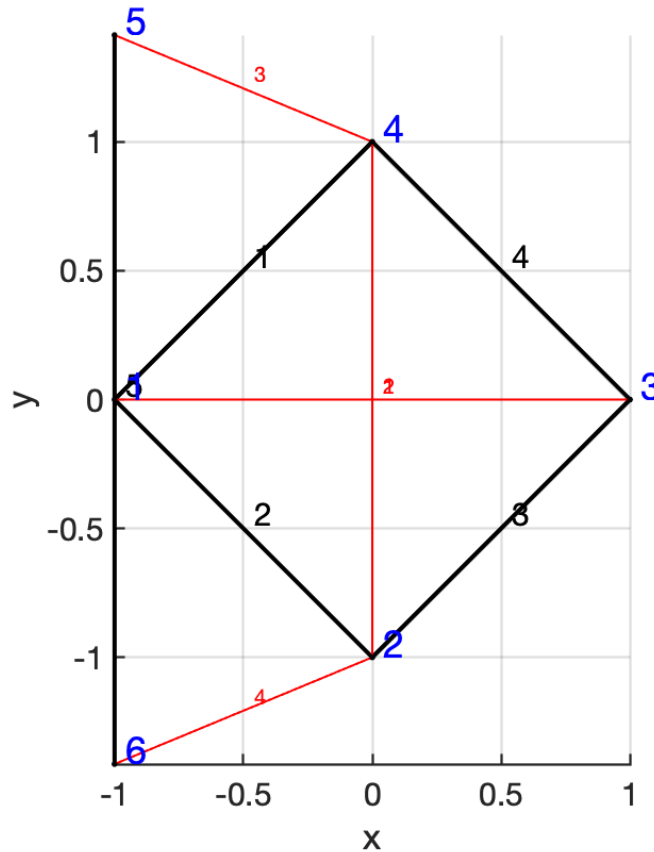


Figure 3.4. Modified D-bar structure

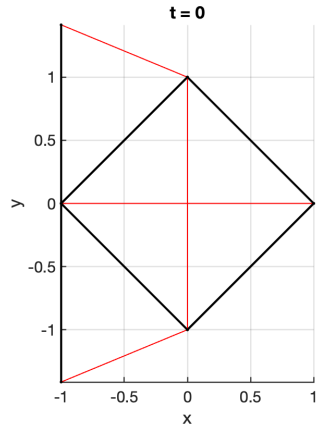
To enhance the controllability of the structure, slight modifications have been made to the basic D-bar structure. As depicted in Figure 3.4, we attached two additional strings to nodes n_2 and n_4 . This has the effect of improving the controllability of the structure in the lateral direction. In addition, we have pinned node n_1 so that it is constrained

to coincide with the point $(-1, 0)$ at all times. Though subtle, these modifications drastically increase the overall reachability of the structure.

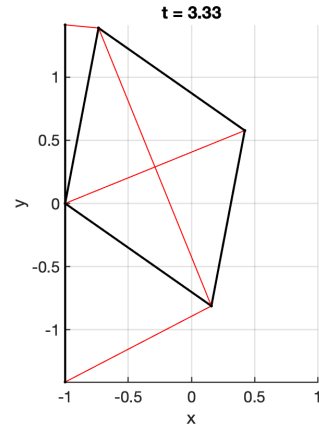
To illustrate, one may briefly consider the basic D-bar structure depicted in Figure 2.8(a). Comprising a total of four Class-2 nodes and only two strings, the basic D-bar is scarcely underactuated. That is, the overall system has a total of eight degrees of freedom and only two actuators. In this type of scenario, the control designer is faced with two options. One can either modify the structure's topology by adding more actuators or decrease the number of control objectives so that the linear programming problem becomes underdetermined. In this case, we have chosen to change the topology of the structure because it is the only way to achieve the control objective. In this example, the control objective matrices are chosen so that the coordinates of node n_3 are driven from the starting position to the point $(0.5, 0.5)$ with unity control gains. That is,

$$\Psi = 1 \quad , \quad \Theta = 1 \quad , \quad \bar{Y} = \begin{bmatrix} 0.5 \\ 0.5 \end{bmatrix} .$$

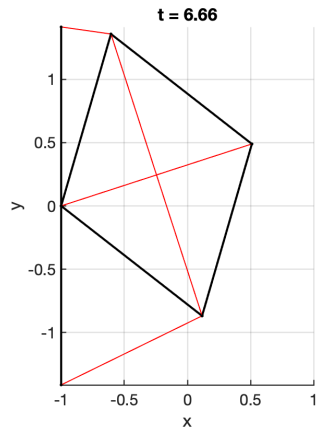
Again, the integration time step is $\Delta t = 0.01$ and we simulate the maneuver for a total time of 10 seconds. A four image time lapse is provided in Figure 3.5. Inspecting Figure 3.5, we can immediately see that the position controller succeeded in driving node n_3 to the desired final location of $(0.5, 0.5)$. This time, however, the controller did overshoot the objective position by roughly 0.1 meters in both x and y directions. This can be seen in Figure 3.6(a). Nonetheless, Figure 3.6(b) shows that static equilibrium was achieved by roughly $t = 8$ seconds. Observing the string force density history in Figure 3.6(c), we can see how string s_3 initially engaged at a force of roughly 1.2 N to pull node n_3 to its target in approximately 2 seconds. At this point, the node overshoots its target, which is why strings s_1 and s_4 engage to return the node to the target position. In future tests, the derivative gain matrix Ψ could be increased to reduce overshoot. In Figure 3.6(d), we see that the residual error of the linear programming problem remained near machine precision for all time steps, which verifies the feasibility of the obtained force densities.



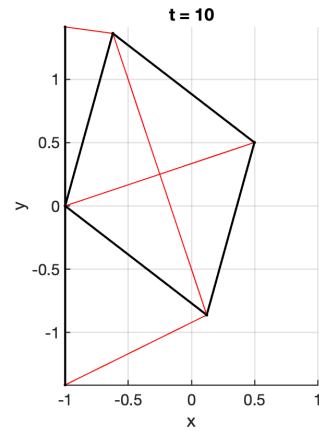
(a) D-bar, $t = 0.00$ seconds



(b) D-bar, $t = 3.33$ seconds

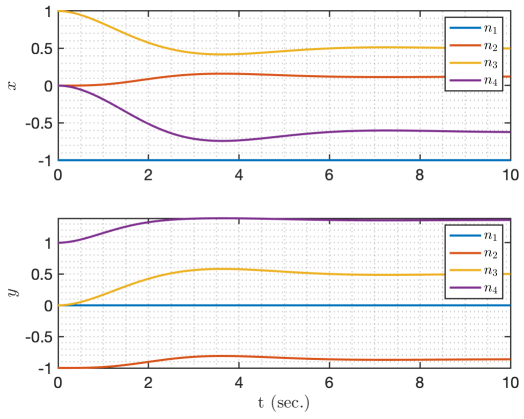


(c) D-bar, $t = 6.66$ seconds

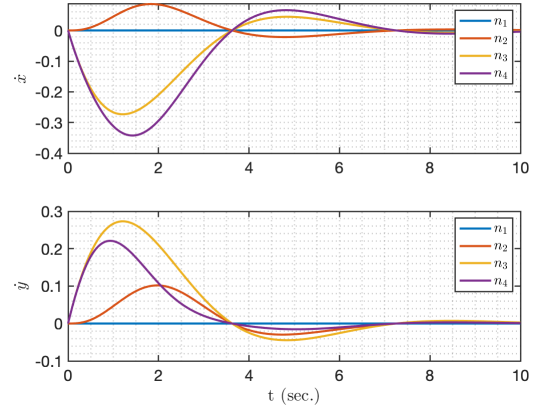


(d) D-bar, $t = 10.00$ seconds

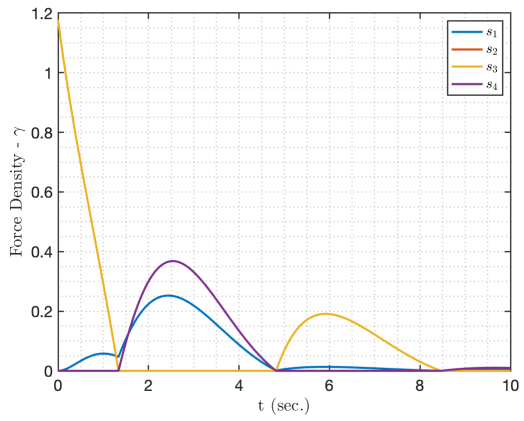
Figure 3.5. D-bar position control sequence



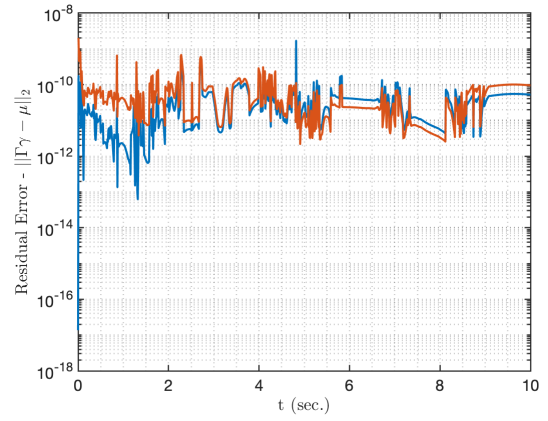
(a) Node position



(b) Node velocity



(c) String force density



(d) Control error residual

Figure 3.6. D-bar position control simulation results

Chapter 4 |

Tensegrity Robotic Arm

In this chapter, a robotic arm is developed based on previous work [46] by combining the fundamental T-bar and D-bar tensegrity structures in a fractal-based realization. The concept of self-similar iterations is utilized to design a dexterous tensegrity robotic arm that could be used to manipulate objects in the environment of outer space. This approach has the benefit of allowing the designer to optimize weight or dexterity by tuning the fractal complexity. To verify the developed control laws, we study the position control of a T2D1 tensegrity structure. The T2D1 robotic arm is constructed by abstracting the basic T-bar structure and replacing the horizontal compressive elements with basic D-bar structures.

We begin the chapter by discussing the concept of self-similar iterations. Several design considerations are proposed for optimizing the weight and deployability of basic two-dimensional structures. We focus mainly on applications for tensegrity robotics. Then, the basic T-bar and D-bar structures are modified, resulting in three-dimensional counterparts for the basic structures. This enables the design and simulation of physically realizable structures. At this point, we return to the simulation environment and initialize the T2D1 robotic arm in its packaged state. By implementing the position control law, we show that we are able to drive the end effector of the robotic arm to a desired location. This example proves the capability of the newly developed control law and shows that it is capable of regulating the shape of complex structures.

4.1 Self-Similar Iterations

Self-similar iterations are the result of replacing a geometrical object with yet another similar geometrical object [3]. We define the iteration complexity q as the number of times the object's components are replaced by itself.

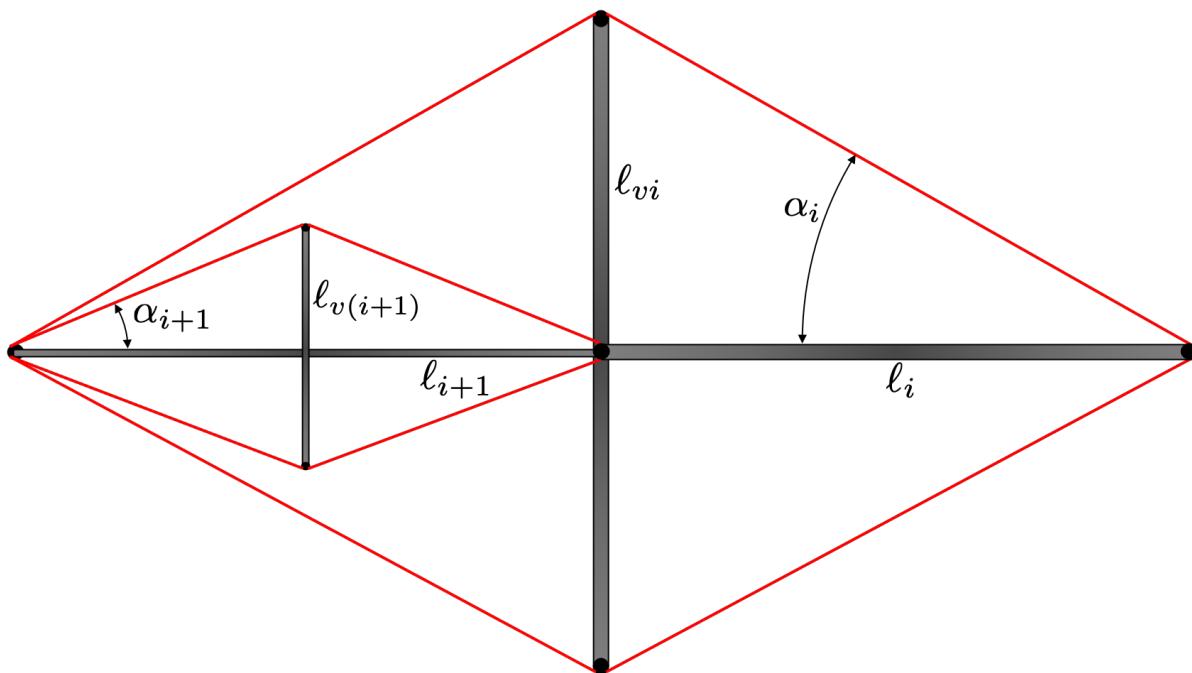


Figure 4.1. T-bar self-similar iterations

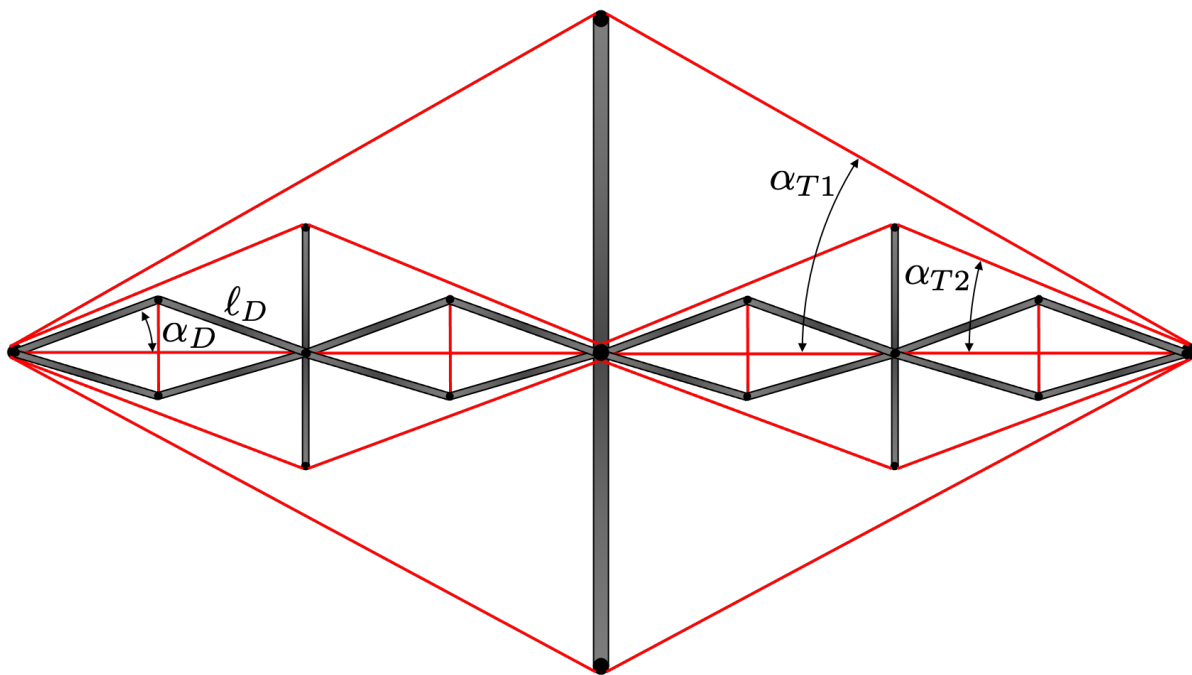


Figure 4.2. Two-dimensional T_2D_1 configuration

As the iteration complexity approaches infinity, the resulting object is called a fractal. Fractals have been a topic of interest in both art and science for many years, and are

often found in biological systems. Sea shells are a common example of this [48]. As such, self-similar iterations have been a common point of interest in the design and optimization of tensegrity structures. The majority of fractal-based tensegrity design has been centered around optimizing the mass efficiency of compressive structures [47]. Our goal here is to extend this area of research by utilizing self-similar iterations to optimize the dexterity of tensegrity robotic arms.

The T-bar structure has been shown to exhibit a higher mass efficiency than the D-bar structure [39]. As such, the T-bar serves as a good starting point for designing a lightweight robotic manipulator. We begin by replacing each horizontal compressive member in the T-bar structure with a similar T-bar structure. This is depicted in Figure 4.1. We define the T-bar complexity q_T as the number of times each compressive member has been replaced by itself. A T-bar with k stages would have complexity $q_T = k$. Several design parameters can be tuned to enhance the mechanical properties of the self-similar T-bar structure. To reduce mass or tune the structural stiffness, the designer may alter the horizontal and vertical bar lengths ℓ_i and ℓ_{vi} as well as change the T-bar angle α_i .

One disadvantage of the T-bar structure is that the horizontal compressive members have a fixed length, making it difficult to efficiently package and deploy the structure. To improve the deployability and overall dexterity of the structure, we replace the horizontal compressive elements in the last stage with a D-bar structure of complexity $q_D = 1$. For a T-bar structure of complexity $q_T = k$, this yields a $T_k D_1$ structure. Figure 4.2 shows the two dimensional representation of of a $T_2 D_1$ tensegrity structure with T-bar angles α_{T1} and α_{T2} , D-bar angle α_D , and D-bar length ℓ_D .

4.2 Three-Dimensional Systems

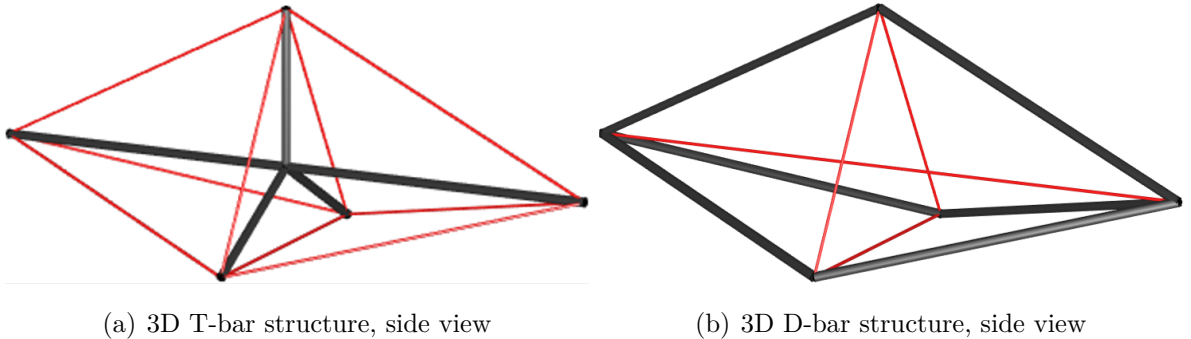


Figure 4.3. Basic three-dimensional structures

Until now, we have only considered tensegrity structures in two dimensions. In the pursuit of designing a physically realizable tensegrity robotic arm, we must extend our developments to three dimensions. One can design three-dimensional extensions of the basic T-bar and D-bar tensegrity structures by maintaining a similar topology and utilizing rotational symmetry. The three-dimensional T-bar structure is depicted in Figure 4.3(a). It has a total of six nodes with five total bar members and nine total string members. At the center of the structure, the five bars connect at a single Class-5 joint, which is modeled as a frictionless ball joint. In the middle of the structure, three string members comprise the outer perimeter to keep tension in the structure. An additional six strings attach the middle of the structure to the two ends in order to maintain static stability.

Figure 4.3(b) depicts the three-dimensional D-bar structure, which comprises a total of five nodes, six total bars and four total strings. There are a total of three Class-2 joints and two Class-3 joints. Three strings forming the outer perimeter of the structure support compressive loading at the end points while one string attaching the ends of the structure maintains stability. The inner string member can also be used to deploy the structure, as we will see in the next section.

4.3 T_2D_1 Robotic Arm Extension

In the following example, we simulate the deployment of a T_2D_1 robotic arm by regulating the positions of certain nodes in the structure. There are a total of 29 nodes in the structure including the four constrained (pinned) nodes at the base of the structure. This results in a total of 75 degrees of freedom in the system. The T_2D_1 robotic arm has a total of 36 bar members and 46 string members. The control objective matrices L and R are chosen specifically to regulate only the x-coordinate of all nodes excluding the four nodes at the base of the structure. Therefore, $L \in \mathbb{R}^{1 \times 3}$ and $R \in \mathbb{R}^{29 \times 25}$. Because there are only 25 control objectives and 46 total strings in the structure, the linear programming problem is underdetermined, which guarantees solutions for the control variable.

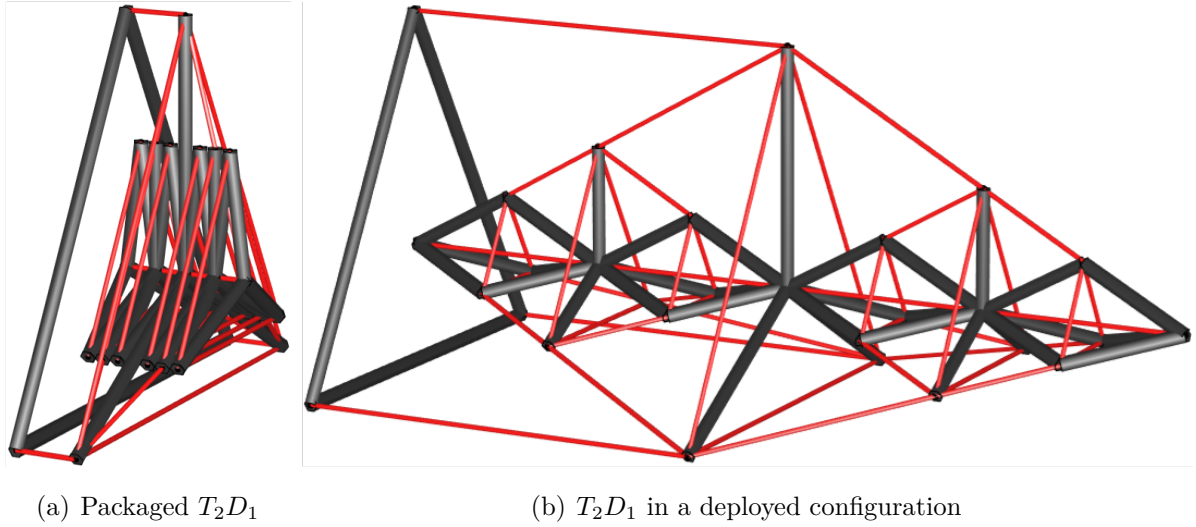


Figure 4.4. T_2D_1 fractal-based robotic arm deployment

For stability purposes, we have chosen to track a sinusoidal shape trajectory from $t = 0$ seconds to $t = 3$ seconds and a 2-second buffer was added to ensure that the desired shape has been reached. In other words, the desired node matrix \bar{Y} was specified so that the end effector n_{23} follows a sinusoidal trajectory from its deployed position to the location $x = 7$. This was done by specifying the position of the end effector as $x(t) = A(\sin(\omega t))$ with amplitude A and frequency ω and using a kinematics model to determine the trajectories of the remaining nodes. The resulting trajectories are depicted in Figure 4.5. The control gains were chosen as $\Psi = 20I$ and $\Theta = 30I$ to reduce the rise time as node coordinates of interest are regulated to the reference trajectory.

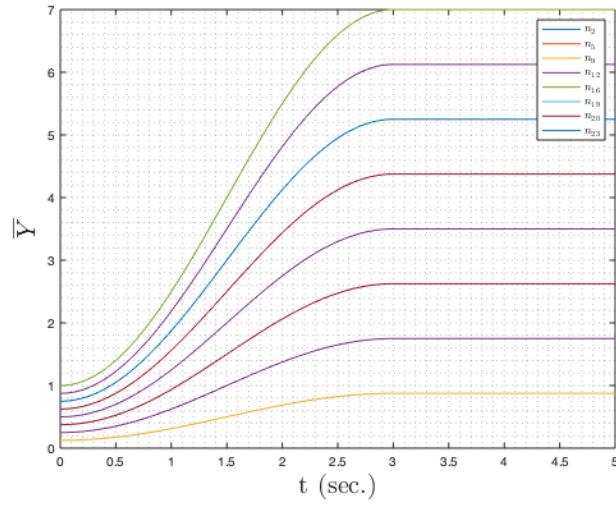
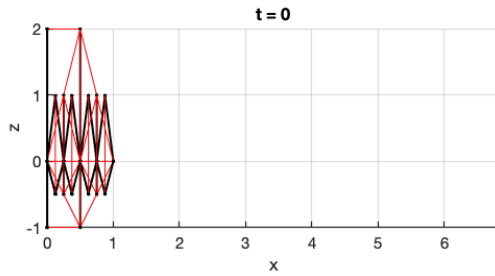
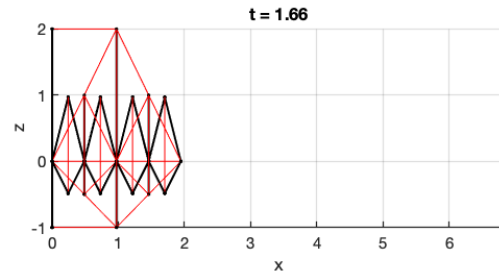


Figure 4.5. Desired node trajectories

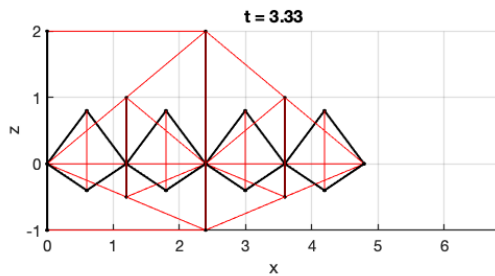
A four image time lapse is provided in Figure 4.6, where we see that the controller succeeded in driving the end effector n_{23} to the desired location of $x = 7$.



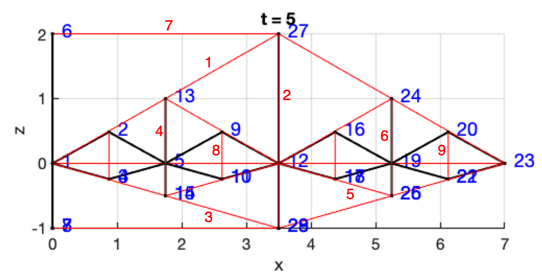
(a) T2D1 arm, $t = 0.00$ seconds



(b) T2D1 arm, $t = 1.66$ seconds



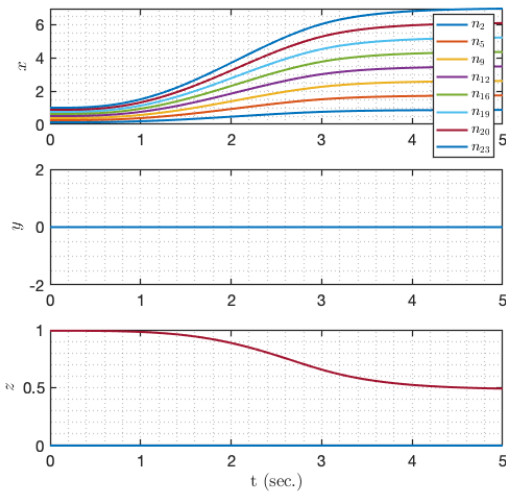
(c) T2D1 arm, $t = 3.33$ seconds



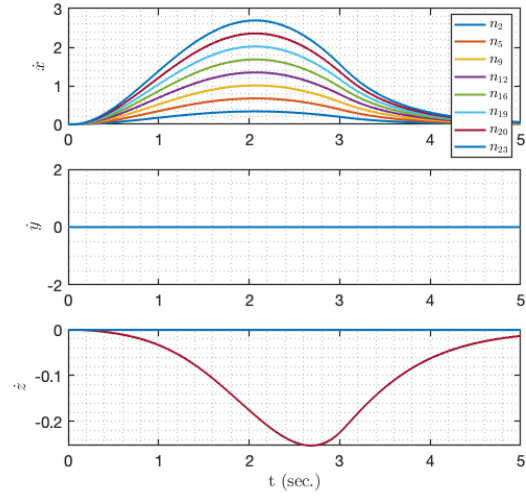
(d) T2D1 arm, $t = 5.00$ seconds

Figure 4.6. T_2D_1 robotic arm position control sequence

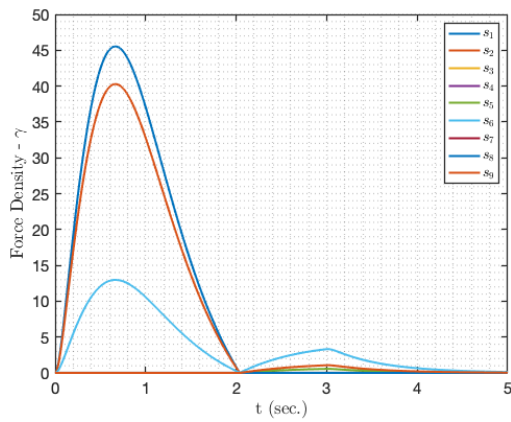
The node position histories are depicted in Figure 4.7(a). Only certain nodes were plotted due to the symmetry of the structure. We can see that all of the plotted nodes maintained $y = 0$ throughout the maneuver while nodes n_2 , n_9 , n_{16} , and n_{20} , which are attached to the D-bars, moved from $z = 1$ to $z = 0.5$. The node velocity histories are plotted in Figure 4.7(b), where we see that the end effector reaches a higher peak velocity than the remaining nodes. The string force density is depicted in Figure 4.7(c). The force density in string s_1 peaks at roughly 45 N/m at $t = 1$ second. Figure 4.7(d) depicts the control law residual error history. The control law error residual is near machine precision, which verifies that the obtained control signal is physically realizable. The string force densities can be uniquely converted back to the physical control variable (string tensions) through a nonlinear transformation.



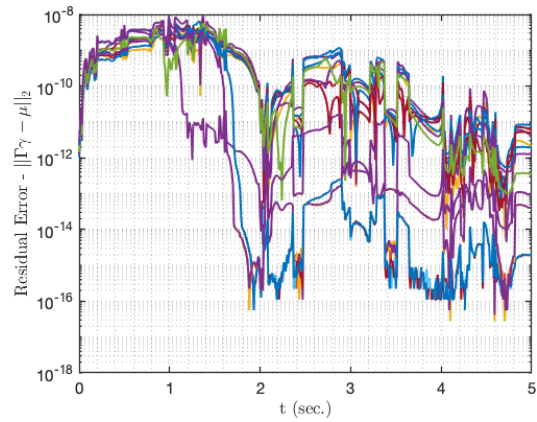
(a) Node position



(b) Node velocity



(c) String force density



(d) Control error residual

Figure 4.7. T_2D_1 robotic arm extension simulation results

Chapter 5 |

Conclusions and Future Work

5.1 Conclusions

In this thesis research, notable progress has been made towards the advancement of space-based tensegrity robotic systems. In Chapter 2, a nonlinear dynamic model has been developed to simulate the dynamics of any structure comprising a network of bar and string members. By representing the dynamics for Class-1 and Class-K tensegrity structures in a non-minimal coordinate system, we were able to avoid the computational errors that can accrue due to the transcendental functions that arise in the minimal coordinates approach. To verify the model, we simulated the dynamics of the double pendulum and showed that the resulting state histories correlate well with the analytical solution. We extended the dynamics model to handle Class-K tensegrity systems by modeling bar-to-bar contact forces and then created a reduced order model to solve for the Lagrange multipliers analytically. As a result, the tensegrity dynamics package is capable of simulating any network of bar and string members. This offers an improvement over pre-existing dynamics models, which are only capable of simulating Class-1 structures. By simulating the free response of two fundamental tensegrity structures, the T-bar and D-bar, we provided preliminary insights into the dynamic behavior of tensegrities about static equilibria. These fundamental results proved to be useful in later simulations.

In Chapter 3, we built upon the developments of Chapter 2 to create a model-based shape control law that uses state feedback to regulate the node positions. We specify control objective matrices to give the designer more freedom in controlling the shape of a given structure. Most notably, this allows the designer to regulate only specific nodes in the structure so that the control law is guaranteed to yield feasible solutions. We derived the error dynamics for position, velocity and acceleration so that they can be controlled simultaneously in a single control law. By defining the control variable as

the force density in the strings, we were able to formulate the equations of motion in control-affine form. This allowed us to formulate the control problem as a linear algebra problem in which convex optimization can be used to solve for the required string force densities at each time step. To guarantee unique solutions, one must specify the control objective matrices specifically so that there are enough strings to perform the desired maneuver. One disadvantage of this approach is that an additional step is required to reproduce the physical control variable (string tensions). However, string tensions can be obtained easily by multiplying the string force density by the string length at each time step.

At the end of Chapter 3, we implemented the shape control law on the fundamental T-bar and D-bar structures. In both cases, we showed that the control law was able to obtain feasible solutions for the string force density by plotting the error residual of the linear algebra problem at each time step. We discovered that, in some cases, the control gains must be tuned to avoid instability in the error dynamics. Instability can occur as a result of commanding large maneuvers between static equilibria. To prevent this from happening, we recommend specifying state trajectories so that the regions of attraction are overlapping between the commanded equilibria. In certain cases, the topology of the structure must be modified to enable the commanded maneuver. For example, the basic D-bar structure comprises only two strings, making it a highly underactuated system. To improve the reachability of the structure, we attached two additional strings. While these modifications to the basic topology can improve overall reachability, the designer should also consider how collision interference due to the added strings can have the opposite effect.

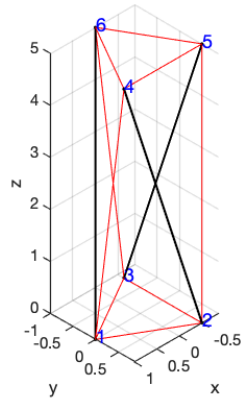
Finally, in Chapter 4, we implemented the model-based control law to change the shape of a very high degree-of-freedom tensegrity robot. A novel T_2D_1 tensegrity robotic arm was introduced as a motivating example for the future of space-based tensegrity structures. We gave a brief overview of self-similar iterations and explained how they can be used to optimize the mass, stiffness and reachability of a tensegrity structure. The T_2D_1 robotic arm was invented by replacing the horizontal compressive elements of the T-bar with basic D-bar structures. This modification improved the overall reachability and deployability of the structure.

To showcase the advancements made in this thesis research, we simulated the deployment of the T_2D_1 robotic arm. With 75 degrees of freedom, this is a very high degree-of-freedom structure, which serves as a test-piece for the future of tensegrity robotics. We showed that our control law is capable of extending the structure from a

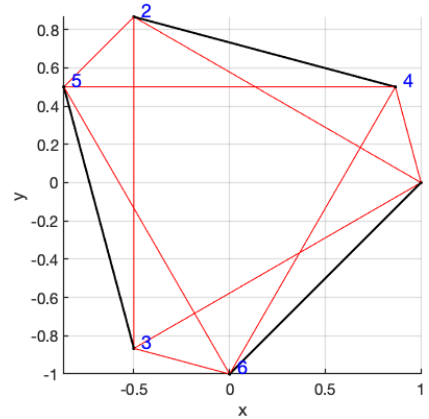
stowed configuration to an extended configuration. In the future, structures like this one could be efficiently packaged in a launch vehicle (at a lower payload cost due to minimum mass) and deployed at a remote destination. Upon arrival, the robotic arm could be used to perform operations such as on-orbit servicing or habitat construction. The robotic arm showcased here is just one of many different applications for deployable tensegrity structures. The future holds great promise for the design and optimization of space-based tensegrity structures.

5.2 Future Work

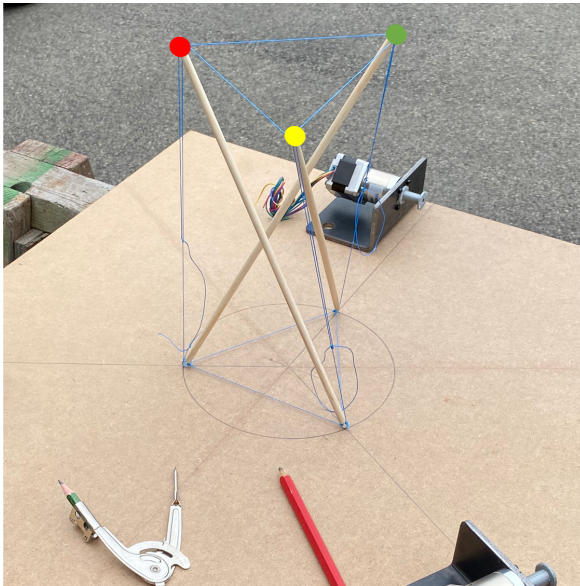
5.2.1 Experimental Verification



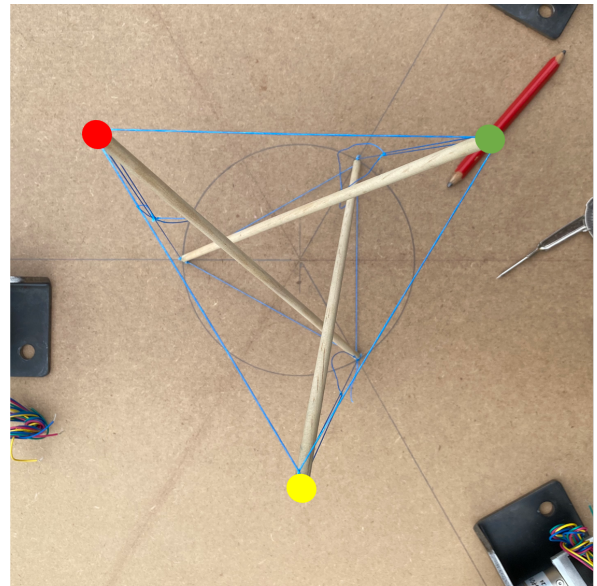
(a) Simulated triplex, side



(b) Simulated triplex, top



(c) Experimental triplex, side



(d) Experimental triplex, top

Figure 5.1. Hardware implementation of the cylindrical triplex

We are currently developing an experimental testbed for the cylindrical triplex tensegrity structure depicted in Figure 5.1. This lab-scale structure will be used to physically verify the model-based shape control law and will serve as a basis for more robust control

strategies.

The cylindrical triplex is one of the most simple 3-dimensional tensegrity topologies, making it a suitable candidate for the transition of control laws from numerical simulation to physical implementation. The triplex is a member of a broader class of cylindrical tensegrity structures, which get their name from the ability to fit inside a cylinder. Since its inception as an art piece, the cylindrical triplex tensegrity has been studied for its potential as a lightweight, space-based, antenna [49]. This has led to developments in the static analysis [50] and numerical form-finding of the triplex's equilibrated shapes [51].

Our goal is to use state feedback to maneuver the triplex between equilibrated shapes. To provide closed-loop feedback of the node positions, a stereo camera will be mounted above the structure, as depicted in Figure 5.2. Based on previous work [52], computer vision will be used to track the (x,y) position of nodes in the structure. Z-position data will be obtained by comparing images taken by the different lenses of the stereo camera. The camera must be placed at an adequate height to account for the focal length of the camera.

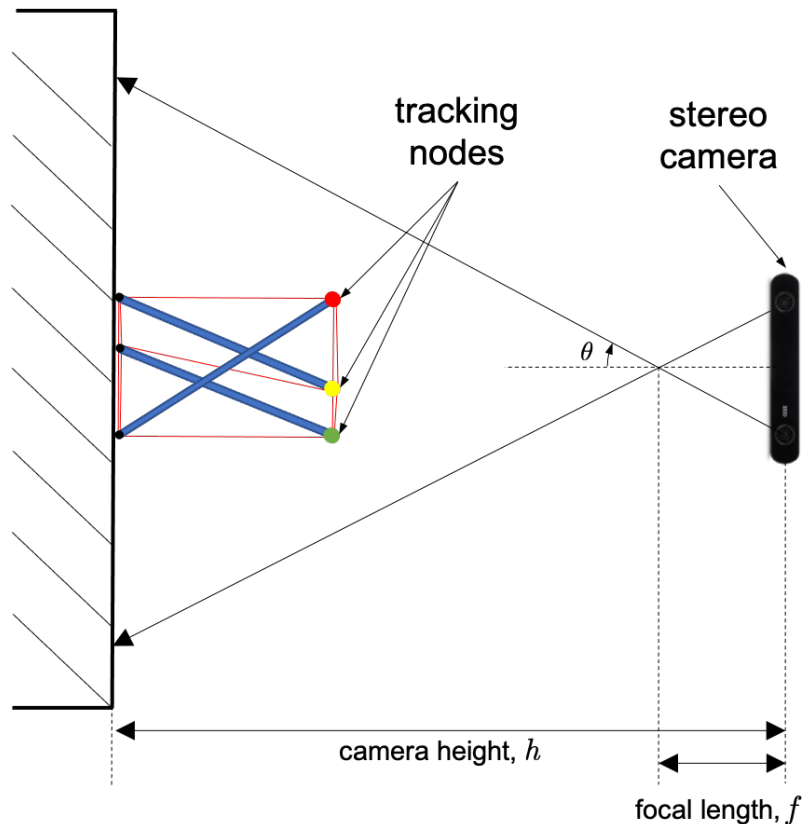


Figure 5.2. Visual feedback of the cylindrical triplex

5.2.2 Optimal and Robust Control Strategies

Although the model-based control law has proven to be successful in computer simulation, additional constraints arise in the physical actuation of tensegrity structures. One such constraint is member interference. Bar and string member collisions will cause un-modeled dynamics to arise in the structure. This could eventually lead to control law instability and even member failure. In the future, it is suggested that a trajectory optimizer is implemented to avoid member collisions. To this end, one may consider solving the corresponding Hamilton-Jacobi-Bellman (HJB) equation to establish a link between reachability and viability [53]

One advantage of having access to physical hardware is the ability to produce input-output data for the system. If a tensegrity structure were to be implemented in outer space, it is undeniable that structural vibrations will propagate throughout the lightly damped string network. To account for these unmodeled dynamics, future work may involve preliminary system identification on the experimental triplex structure. Several approaches exist for the identification of linear and time-varying linear systems [54–56]. Though it is not currently understood whether these algorithms would capture the nonlinear dynamics of tensegrity systems.

Appendix A | Elastic String Modeling

We prescribe tension in a given string by stretching it beyond its rest length. Assuming that strings are Hookean and follow a viscous friction damping model, the tension in the i th string is written as

$$\|t_i\| = k_i (\|s_i\| - \rho_i) + z_i \frac{s_i^T \dot{s}_i}{\|s_i\|} \quad (\text{A.1})$$

where ρ_i is the rest length of the i th string, k_i is the extensional stiffness, z_i is the damping constant, and s_i is the string vector written in inertial coordinates. In this work, the control variable is defined as the string ‘force density’. We arrive at the string force density in the i th string by simply dividing the tension by the length of the string as

$$\gamma_i = \frac{\|t_i\|}{\|s_i\|} = k_i \left(1 - \frac{\rho_i}{\|s_i\|}\right) + z_i \frac{s_i^T \dot{s}_i}{\|s_i\|^2}. \quad (\text{A.2})$$

If $\rho_i > \|s_i\|$, Eq. (A.2) yields a negative value and the string tension should be set to zero, as a string can never push along its length. Now, writing Eqs. (A.1) and (A.2) in matrix form, we have

$$\begin{aligned} \hat{\gamma} &= \left(I - [S^T S]^{-\frac{1}{2}} \hat{\rho}\right) \hat{k} + [S^T \dot{S}] [S^T S]^{-1} \hat{z}, \\ T &= S \hat{\gamma} = S \left(I - [S^T S]^{-\frac{1}{2}} \hat{\rho}\right) \hat{k} + S [S^T \dot{S}] [S^T S]^{-1} \hat{z}. \end{aligned} \quad (\text{A.3})$$

where the i th column of T is the string tension vector in the i th string. Eq. (A.3) can be written more compactly as

$$T = S \hat{\gamma} = (S - S_0) \hat{k} + S [S^T \dot{S}] [S^T S]^{-1} \hat{z} \quad (\text{A.4})$$

where $S_0 = S [S^T S]^{-\frac{1}{2}} \hat{\rho}$ represents the matrix containing the rest length vectors

Appendix B | Tensegrity Dynamics Flow Charts

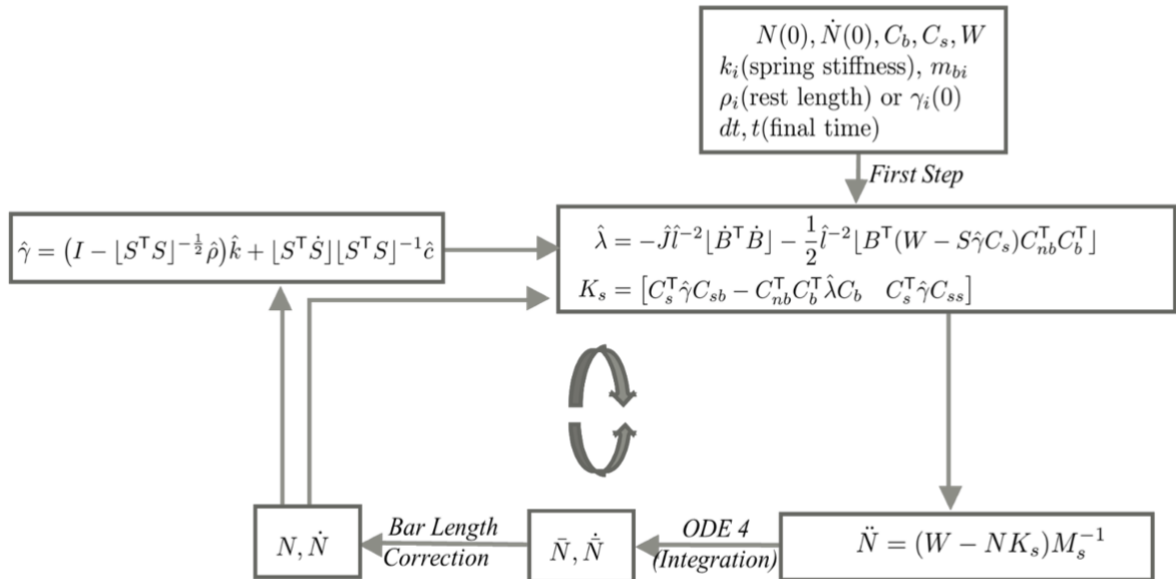


Figure B.1. Class-1 dynamics flow chart

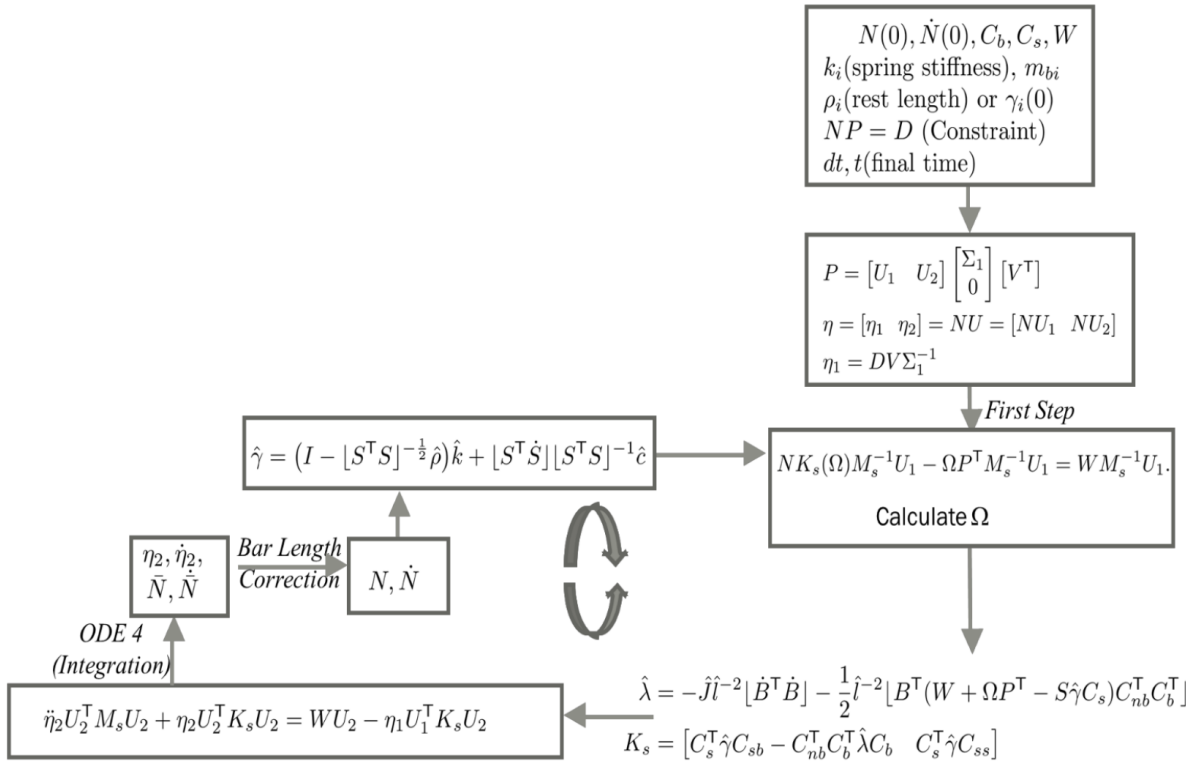


Figure B.2. Class-k dynamics flow chart

Appendix C | Analytical Solution for the Class-K Lagrange Multiplier

Our goal is to solve analytically for the $3 \times c$ matrix of Lagrange multipliers Ω that satisfies the system dynamics and c Class-k constraints. The developments here come directly from [20]. We proceed by substituting K and $\hat{\lambda}$ into the constraint equation (Eq. (2.48)) to write the equation in terms of Ω and known variables only. Then, we separate the known variables from the coefficients of Ω and solve for the constraint multipliers in a linear algebra problem.

Lemma 1 *The Lagrange multiplier that satisfies Eq. (2.48) can be computed as*

$$\begin{bmatrix} \omega_1 \\ \omega_2 \\ \vdots \\ \omega_c \end{bmatrix} = \left(\sum_{i=1}^{\beta} \frac{1}{2l_i^2} \mathcal{C}_{:,i}^T \otimes (b_i \otimes (b_i \mathcal{D}_{i,:})^T) - \begin{bmatrix} \mathcal{E} \otimes e_1^T \\ \mathcal{E} \otimes e_2^T \\ \mathcal{E} \otimes e_3^T \end{bmatrix} \right)^{-1} \begin{bmatrix} \mathcal{A}_{1,:}^T \\ \mathcal{A}_{2,:}^T \\ \mathcal{A}_{3,:}^T \end{bmatrix}, \quad (\text{C.1})$$

where ω_i is the i th column of Ω , $\mathcal{C} = P^T C_b^T$, $\mathcal{D} = C_b M_s^{-1} U_1$, $\mathcal{E} = P^T M_s^{-1} U_1$, $\mathcal{A} = -S \hat{\gamma} C_s M_s^{-1} U_1 + B \left[\frac{1}{2} \hat{l}^{-2} B^T (S \hat{\gamma} C_s - W) C_b^T - \hat{l}^{-2} \hat{J} \dot{B}^T \dot{B} \right] C_b M_s^{-1} U_1 + W M_s^{-1} U_1 \in \mathbb{R}^{3 \times c}$, and \otimes denotes the Kronecker Product [57].

Proof We begin by substituting Eq. (2.41c) into Eq. (2.48) as

$$N \left(C_s^T \hat{\gamma} C_s - C_b^T \hat{\lambda} C_b \right) M^{-1} U_1 - \Omega P^T M^{-1} U_1 = W M^{-1} U_1 \quad (\text{C.2})$$

Further substituting $B = N C_b^T$ and $S = N C_s^T$, and expanding:

$$S\hat{\gamma}C_sM^{-1}U_1 - B\hat{\lambda}C_bM^{-1}U_1 - \Omega P^T M^{-1}U_1 = WM^{-1}U_1 \quad (\text{C.3})$$

Now, substituting Eq. (2.41d) into Eq. (C.3) yields

$$\begin{aligned} & \frac{1}{2}B \left[\hat{l}^{-2}B^T \Omega P^T C_b^T \right] C_b M_s^{-1}U_1 - \Omega P^T M^{-1}U_1 \\ &= -S\hat{\gamma}C_sM^{-1}U_1 + B \left[\frac{1}{2}\hat{l}^{-2}B^T (S\hat{\gamma}C_s - W) C_b^T - \hat{l}^{-2}\hat{J}\hat{B}^T\hat{B} \right] C_b M_s^{-1}U_1 \\ & \quad + WM^{-1}U_1 = \mathcal{A} \quad (\text{C.4}) \end{aligned}$$

By defining $\mathcal{C} = P^T C_b^T$, $\mathcal{D} = C_b M_s^{-1}U_1$, $\mathcal{E} = P^T M_s^{-1}U_1$, Eq. (C.4) can be written in terms of Ω and known variables only as

$$\frac{1}{2}B \left[\hat{l}^{-2}B^T \Omega \mathcal{C} \right] \mathcal{D} - \Omega \mathcal{E} = \mathcal{A} \quad (\text{C.5})$$

In order to solve for the Lagrange multipliers, Ω must first be broken down into $\Omega = [\omega_1 \ \omega_2 \ \dots \ \omega_c] \in \mathbb{R}^{3 \times c}$ as

$$\mathcal{F} = \frac{1}{2} \left[\hat{l}^{-2}B^T \Omega \mathcal{C} \right] = \begin{bmatrix} \ddots & 0 & 0 \\ 0 & \sum_{j=1}^c \frac{\mathcal{C}_{j,i}}{2l_i^2} b_i^T \omega_j & 0 \\ 0 & 0 & \ddots \end{bmatrix} \quad (\text{C.6})$$

Therefore, the element on the m th row and n th column of the matrix $\mathcal{G} = \frac{1}{2}B \left[\hat{l}^{-2}B^T \Omega \mathcal{C} \right] \mathcal{D}$, for $m \in \{1, 2, 3\}$ and $n \in \{1, 2, \dots, c\}$ is

$$\mathcal{G}_{m,n} = b_{m,1}\mathcal{F}_{1,1}\mathcal{D}_{1,n} + b_{m,2}\mathcal{F}_{2,2}\mathcal{D}_{2,n} + \dots + b_{m,\beta}\mathcal{F}_{\beta,\beta}\mathcal{D}_{\beta,n} = \sum_{j=1}^c \sum_{i=1}^{\beta} b_{m,i}\mathcal{D}_{i,n} \frac{\mathcal{C}_{j,i}}{2l_i^2} b_i^T \omega_j. \quad (\text{C.7})$$

Similarly, the second term in Eq. (C.5) can be expanded as

$$\Omega \mathcal{E} = [\omega_1 \ \omega_2 \ \dots \ \omega_c] \mathcal{E} = \omega_1 \mathcal{E}_{1,:} + \omega_2 \mathcal{E}_{2,:} + \dots + \omega_c \mathcal{E}_{c,:} = \sum_{j=1}^c \omega_j \mathcal{E}_{j,:}. \quad (\text{C.8})$$

The element on the m th row and n th column of this matrix is

$$(\Omega\mathcal{E})_{m,n} = \sum_{j=1}^c e_m^T \omega_j \mathcal{E}_{j,n} = \sum_{j=1}^c \mathcal{E}_{j,n} e_m^T \omega_j. \quad (\text{C.9})$$

Now, substituting the (m,n) th element from Eq. (C.7) and Eq. (C.9) into Eq. (C.5) yields

$$\begin{aligned} & \sum_{j=1}^c \sum_{i=1}^{\beta} b_{m,i} \mathcal{D}_{i,n} \frac{\mathcal{C}_{j,i}}{2l_i^2} b_i^T \omega_j - \sum_{j=1}^c \mathcal{E}_{j,n} e_m^T \omega_j = \mathcal{A}_{m,n} \\ \Rightarrow & \sum_{j=1}^c \left(\sum_{i=1}^{\beta} \frac{b_{m,i} \mathcal{D}_{i,n} \mathcal{C}_{j,i}}{2l_i^2} b_i^T - \mathcal{E}_{j,n} e_m^T \right) \omega_j = \mathcal{A}_{m,n}. \end{aligned} \quad (\text{C.10})$$

This can be rearranged into the matrix equation:

$$\Theta^{3c \times 3c} \begin{bmatrix} \omega_1 \\ \omega_2 \\ \vdots \\ \omega_{n_c} \end{bmatrix} = \begin{bmatrix} \mathcal{A}_{1,:}^T \\ \mathcal{A}_{2,:}^T \\ \vdots \\ \mathcal{A}_{3,:}^T \end{bmatrix} \quad (\text{C.11})$$

where

$$\begin{aligned} \begin{bmatrix} \mathcal{A}_{1,:}^T \\ \mathcal{A}_{2,:}^T \\ \mathcal{A}_{3,:}^T \end{bmatrix} &= \begin{bmatrix} \sum_{i=1}^{\beta} \frac{b_{1,i} \mathcal{C}_{1,i}}{2l_i^2} \mathcal{D}_{i,:} b_i^T & \sum_{i=1}^{\beta} \frac{b_{1,i} \mathcal{C}_{2,i}}{2l_i^2} \mathcal{D}_{i,:} b_i^T & \cdots & \sum_{i=1}^{\beta} \frac{b_{1,i} \mathcal{C}_{c,i}}{2l_i^2} \mathcal{D}_{i,:} b_i^T \\ \sum_{i=1}^{\beta} \frac{b_{2,i} \mathcal{C}_{1,i}}{2l_i^2} \mathcal{D}_{i,:} b_i^T & \sum_{i=1}^{\beta} \frac{b_{2,i} \mathcal{C}_{2,i}}{2l_i^2} \mathcal{D}_{i,:} b_i^T & \cdots & \sum_{i=1}^{\beta} \frac{b_{2,i} \mathcal{C}_{c,i}}{2l_i^2} \mathcal{D}_{i,:} b_i^T \\ \sum_{i=1}^{\beta} \frac{b_{3,i} \mathcal{C}_{1,i}}{2l_i^2} \mathcal{D}_{i,:} b_i^T & \sum_{i=1}^{\beta} \frac{b_{3,i} \mathcal{C}_{2,i}}{2l_i^2} \mathcal{D}_{i,:} b_i^T & \cdots & \sum_{i=1}^{\beta} \frac{b_{3,i} \mathcal{C}_{c,i}}{2l_i^2} \mathcal{D}_{i,:} b_i^T \end{bmatrix} \\ &\quad \times \begin{bmatrix} \omega_1 \\ \omega_2 \\ \vdots \\ \omega_c \end{bmatrix} - \begin{bmatrix} \mathcal{E}_{1,:}^T e_1^T & \mathcal{E}_{2,:}^T e_1^T & \cdots & \mathcal{E}_{c,:}^T e_1^T \\ \mathcal{E}_{1,:}^T e_2^T & \mathcal{E}_{2,:}^T e_2^T & \cdots & \mathcal{E}_{c,:}^T e_2^T \\ \mathcal{E}_{1,:}^T e_3^T & \mathcal{E}_{2,:}^T e_3^T & \cdots & \mathcal{E}_{c,:}^T e_3^T \end{bmatrix} \begin{bmatrix} \omega_1 \\ \omega_2 \\ \vdots \\ \omega_c \end{bmatrix}, \end{aligned} \quad (\text{C.12})$$

$$\begin{bmatrix} \mathcal{A}_{1,:}^T \\ \mathcal{A}_{2,:}^T \\ \mathcal{A}_{3,:}^T \end{bmatrix} = \left(\left[\sum_{i=1}^{\beta} \frac{\mathcal{C}_{1,i}}{2l_i^2} b_i \otimes (b_i \mathcal{D}_{i,:})^T \quad \sum_{i=1}^{\beta} \frac{\mathcal{C}_{2,i}}{2l_i^2} b_i \otimes (b_i \mathcal{D}_{i,:})^T \quad \cdots \quad \sum_{i=1}^{\beta} \frac{\mathcal{C}_{c,i}}{2l_i^2} b_i \otimes (b_i \mathcal{D}_{i,:})^T \right] \right)$$

$$- \begin{pmatrix} \mathcal{E} \otimes e_1^T \\ \mathcal{E} \otimes e_2^T \\ \mathcal{E} \otimes e_3^T \end{pmatrix} \begin{bmatrix} \omega_1 \\ \omega_2 \\ \vdots \\ \omega_c \end{bmatrix}, \quad (\text{C.13})$$

$$\begin{bmatrix} \mathcal{A}_{1,:}^T \\ \mathcal{A}_{2,:}^T \\ \mathcal{A}_{3,:}^T \end{bmatrix} = \underbrace{\left(\sum_{i=1}^{\beta} \frac{1}{2l_i^2} \mathcal{C}_{:,i}^T \otimes (b_i \otimes (b_i \mathcal{D}_{i,:})^T) \right)}_{\Theta^{3c \times 3c}} - \begin{pmatrix} \mathcal{E} \otimes e_1^T \\ \mathcal{E} \otimes e_2^T \\ \mathcal{E} \otimes e_3^T \end{pmatrix} \begin{bmatrix} \omega_1 \\ \omega_2 \\ \vdots \\ \omega_c \end{bmatrix}. \quad (\text{C.14})$$

The above linear algebra problem represents $3c$ equations for $3c$ unknowns and can be solved for the Lagrange multipliers by taking the inverse.

Bibliography

- [1] NASA, *FY 2022: NASA Budget Request*, 28 May 2021.
- [2] S. Jackson, *Competition Seeks University Concepts for Gateway and Deep Space Exploration Capabilities*, nasa.gov, 11 September 2018.
- [3] R. Skelton and M. de Oliviera, *Tensegrity Systems*, Springer, pp. 1-43, 2009.
- [4] R. B. Fuller., *Tensile integrity structures*, United States Patent Office, 1959, US patent 3.063.521.
- [5] Gómez-Jáuregui, V. (2009), *Controversial Origins of Tensegrity*, Proceedings of the IASS Symposium 2009.
- [6] S. Wendling, C. Oddou, and D. Isabey, *Stiffening response of a cellular tensegrity*. Journal of Theoretical Biology, 196:309–325, 1999.
- [7] C. Sultan, D. Stamenović, and D. Ingber, *A computational tensegrity model predicts dynamic rheological behaviors in living cells*, Annals of Biomedical Engineering, 32(4):520–530, 2004.
- [8] A. Simmons, C. Michal, and L. Jelinski, *Molecular orientation and two-component nature of the crystalline fraction of dragline silk*. Science, 271:84–87, 1996.
- [9] S. M. Levin, *Putting the shoulder to the wheel: A new biomechanical model for the shoulder girdle*, Biomed. Sci. Instrum., vol. 33, pp. 412–417, 1997.
- [10] S. M. Levin, *The tensegrity-truss as a model for spine mechanics: Biotensegrity*, J. Mechanics Medicine Biol., vol. 02, no. 03n04, pp. 375–388, 2002.
- [11] D. E. Ingber, *The architecture of life*, Scientific America, vol. 278, no. 1, pp. 48–57, 1998.

- [12] Civic Arts Project, *Needle Tower*, civicartsproject.com, 2021, web.
- [13] S. Markin, M. Lemay, B. Prilutsky, and I. Rybak, *Motoneuronal and muscle synergies involved in cat hindlimb control during fictive and real locomotion: a comparison study*, *The Journal of Neurophysiology*, 2012.
- [14] S. Pellegrino, *Deployable structures*, vol. 412, Springer, 2014.
- [15] G. Tibert, *Deployable tensegrity structures for space applications*, Doctoral Thesis, KTH, 2002.
- [16] C. Sultan and R. T. Skelton, *Tendon control deployment of tensegrity structures*, *Smart Structures and Materials 1998: Mathematics and Control in Smart Structures*, 3323, pp. 455–467.
- [17] D. Williamson, R.E. Skelton, J. Han, *Equilibrium Conditions of a Tensegrity Structure*, *International Journal of Solids and Structures*, 7 July 2003.
- [18] K. Roffman, *Shape Change and Structural Performance of Cable-Actuated Cylindrical Tensegrities*, M.S. Thesis, Aerospace Engineering Dept., Pennsylvania State Univ., State College, PA, 2018.
- [19] H. Murakami, *Static and dynamic analyses of tensegrity structures. part 1. nonlinear equations of motion*, *International Journal of Solids and Structures*, vol. 38(20), pp. 3599–3613, 2001.
- [20] R. Goyal and R. E. Skelton, *Tensegrity system dynamics with rigid bars and massive strings*, *Multibody Syst. Dyn.*, vol. 46, no. 3, pp. 209-212, 2019.
- [21] Z. Kan, H. Peng, and B. Chen, *Complementarity framework for nonlinear analysis of tensegrity structures with slack cables*, *AIAA Journal*, vol. 56, no. 12, pp. 5013–5027, 2018.
- [22] D. Fadeyev, A. Zhakatayev, A. Kuzdeuov, and H. A. Varol, *Generalized dynamics of stacked tensegrity manipulators*, *IEEE Access*, vol. 7, pp. 63 472–63 484, 2019.
- [23] H. Peng, F. Li, and Z. Kan, *A novel distributed model predictive control method based on a substructuring technique for smart tensegrity structure vibrations*, *Journal of Sound and Vibration*, January 2020.

- [24] G. Lai, A. Plummer and D. Cleaver, *Distributed Actuation and Control of a Morphing Tensegrity Structure*, ASME Journal of Dynamic Systems, Measurement, and Control, 2020.
- [25] A. Iscen, A. Agogino, V. SunSpiral, and K. Tumer, *Controlling tensegrity robots through evolution*, GECCO 2013 - Proceedings of the 2013 Genetic and Evolutionary Computation Conference, pp. 1293-1300, 2013.
- [26] V. SunSpiral, A. Agogino, and D. Atkinson, *Final Report Phase II, Super Ball Bot - Structures for Planetary Landing and Exploration*, NASA Innovative Advanced Concepts Program, September, 2015.
- [27] B. Chen and H. Jiang, *Swimming performance of a tensegrity robotic fish*, Soft Robot., vol. 6, no. 4, pp. 520–531, 2019.
- [28] S. Lessard, D. Castro, W. Asper, S. Deep Chopra, L. Breanna Baltaxe-Admony, M. Teodorescu, V. SunSpiral, and A. Agogino, *A bio-Inspired Tensegrity Manipulator with Multi-DOF, Structurally Compliant Joints*, in Proc. IEEE/RSJ Int. Conf. Intell. Robots Syst., pp. 5515–5520, 2016.
- [29] W. Li, H. Nabae, G. Endo, and K. Suzumori, *New Soft Robot Hand Configuration with Combined Biotensegrity and Thin Artificial Muscle*, IEEE Robotics and Automation Letters, Vol. 5, No. 3, July 2020.
- [30] J. Sun, G. Song, J. Chu, and L. Ren, *An Adaptive Bioinspired Foot Mechanism Based on Tensegrity Structures*, Soft Robot., vol. 6, no. 6, pp. 778–789, Jan. 2019.
- [31] J. W. Gibbs, *Elements of Vector Analysis*, p. 67, 1884.
- [32] P.C. Hughes, *Spacecraft Attitude Dynamics*, Wiley & Sons, New York, 1986.
- [33] H. Schaub and J. L. Junkins, *Analytical Mechanics of Space Systems*, AIAA Education Series, Reston, VA, 2003.
- [34] K. Nagase and R.E. Skelton, *Network and vector forms of tensegrity system dynamics*, Mech. Res. Commun. 59, pp. 14-25, 2014.
- [35] A.A. Shavana, *Dynamics of Multibody Systems*, Cambridge University Press, 2005.
- [36] R.C. Hibbeler, *Engineering Mechanics: Statics and Dynamics, 14/e*, Prentice Hall, 2012.

- [37] J. Cheong and R.E. Skelton, *Nonminimal dynamics of general class k tensegrity systems*, Int. J. Struct. Stab. Dyn. 15(2), 1450042, 2015.
- [38] R. Goyal, M. Chen, M. Majji, and R.E. Skelton, *MOTES: Modeling of Tensegrity Structures*, Journal of Open Source Software, 2019.
- [39] R. Goyal, R.E Skelton, and E. A. Peraza Hernandez, *Design of minimal mass load-bearing tensegrity lattices*, Mechanics Research Communications, vol. 103, p. 103477, 2020.
- [40] J. Henrickson, R.E. Skelton, and John Valasek, *Shape Control of Tensegrity Structures*, AIAA SPACE, pp. 6-8, 2015.
- [41] A. Isidori, *Nonlinear Control Systems, 2nd Ed.*, Springer-Verlag, Berlin, 1989.
- [42] S. Sastry, *Nonlinear Systems: Analysis, Stability, and Control*, Springer-Verlag, Berlin, 1999.
- [43] H. K. Khalil, *Nonlinear Systems*, Macmillan, New York, pp. 111-181, 2002.
- [44] M. Grant and S. Boyd, *CVX: Matlab software for disciplined convex programming*, version 2.0 beta, September 2013.
- [45] M. Grant and S. Boyd. *Graph implementations for nonsmooth convex programs*, *Recent Advances in Learning and Control (a tribute to M. Vidyasagar)*, V. Blondel, S. Boyd, and H. Kimura, editors, pp. 95-110, Lecture Notes in Control and Information Sciences, Springer, 2008.
- [46] R. Goyal, M. Majji and R.E. Skelton, *Model-based Shape Control of Tensegrity Robotic Systems*, arXiv: Robotics, 2020.
- [47] U. Boz, R. Goyal and R.E. Skelton, *Actuators and Sensors Based on Tensegrity D-bar Structures*, Front. Astron. Space Sci., 2018.
- [48] M. S. Malone, *God, Stephen Wolfram, and everything else*, Forbes ASAP, November 27, 2000.
- [49] K. Yildiz, *Cable Actuated Tensegrity Structures for Deployable Space Booms with Enhanced Stiffness*, Ph.D. Dissertation, Aerospace Engineering Dept., Pennsylvania State Univ., State College, PA, 2018.

- [50] G. Estrada, H. Bungartz, and C. Mohrdieck *On Cylindrical Tensegrity Structures*, Proceedings of the 5th International Conference on Computation of Shell and Spatial Structures Salzburg, Austria, 2005.
- [51] K. Roffman and G. Lesieutre, *Shape Change Analysis of Cable-Actuated Cylindrical Tensegrity Structures*, AIAA Scitech Forum, 2019.
- [52] H. Karnan, R. Goyal, M. Majji, R.E. Skelton, and P. Singla *Visual Feedback Control of Tensegrity Robotic Systems*, International Conference on Intelligent Robots and Systems (IROS), September, 2017.
- [53] J. Lyergos, *On reachability and minimum cost optimal control*, Automatica, 40(6), pp. 917–927.
- [54] J. Juang and R. Pappa, *An Eigensystem Realization Algorithm for Modal Parameter Identification and Model Reduction*, AIAA Journal of Guidance, Control, and Dynamics, 1984.
- [55] J. Juang, M. Phan, L. Horta, and R. Longman, *Identification of Observer/Kalman Filter Markov Parameters: Theory and Experiments*, AIAA Journal of Guidance, Control, and Dynamics, 1993.
- [56] M. Majji, J. Juang and J. Junkins, *Time-Varying Eigensystem Realization Algorithm*, AIAA Journal of Guidance, Control, and Dynamics, 2010.
- [57] G. Zehfuss, *Ueber eine gewisse Determinante*, Zeitschrift für Mathematik und Physik, 1858

Nathaniel S. Osikowicz

AEROSPACE ENGINEER · ROCK CLIMBING GUIDE

✉ nko5048@psu.edu | 🏠 natesosikowicz.wixsite.com/curriculumvitae | 📺 nateosik

Education

The Pennsylvania State University | The Schreyer Honors College

THE COLLEGE OF ENGINEERING | BACHELOR OF SCIENCE IN AEROSPACE ENGINEERING

University Park, PA

Anticipated: May 2021

The Pennsylvania State University | Integrated Undergraduate-Graduate Program

THE COLLEGE OF ENGINEERING | MASTER OF SCIENCE IN AEROSPACE ENGINEERING

University Park, PA

Anticipated: May 2021

Academic Experience

Control and Analysis of Stochastic Systems (CASS) Lab

RESEARCH ASSISTANT

- Investigate the biological principle of tensegrity and its applications to dexterous manipulation
- Implemented a model-based shape control law to maneuver tensegrity robots by controlling the tensions in supporting tendons
- Realize optimal dexterity manipulator configurations through bio-inspired fractal-based design
- Investigate a robust, data-driven, tensegrity shape control framework to dampen structural vibrations based on the Observer Kalman-Filter Identification (OKID)
- Construct a hardware-in-the-loop testbed for implementing tensegrity shape control algorithms

University Park, PA

May 2019 - Present

Aerial Autonomy Senior Design Competition

AUTONOMY ENGINEER

- Managed a team of 6 students in the agile development of a GPS-denied autonomous UAV
- Architected 6DOF Extended Kalman Filter (EKF) for computer vision-based autonomous landing
- Developed Hardware-in-the-Loop (HITL) simulation environment for attitude control system testing
- Refined sensor processing algorithms for LiDAR and IMU measurements

University Park, PA

September 2019 - May 2020

Work Experience

Lockheed Martin Space Systems

ENGINEERING INTERN

- Recognized for 'best 2019 intern presentation' on vehicle state estimation and the mental model
- Co-developed the curriculum for the Spring 2020 Motor Controls Course
- Architected software to predict and prevent iron nitrate accumulation on MILSTAR satellite thrusters

Sunnyvale, CA

May 2019 - August 2019

Uniflight Global Inc.

HELICOPTER TECHNICIAN

- Developed sheet metal provisions for the Bell 429 GlobalRanger rotorcraft
- Conducted weight & balance evaluations for a variety of rotorcraft
- Devised shipping methods for the Agusta A109E transmission assembly

Belle Vernon, PA

June 2018 - August 2018

Leadership Experience

The American Institute of Aeronautics and Astronautics

PRESIDENT, PENN STATE CHAPTER

- Launched the control system design series for undergraduates interested in microcontrollers
- Managed an executive board through strategic event planning and budgeting efforts
- Implemented a framework for professional development among Aerospace Engineering students

University Park, PA

April 2018 - May 2020

Penn State Outdoor Adventures

ROCK CLIMBING GUIDE

- Plan, prepare and guide rock climbing excursions for 5-10 participants in the Eastern United States
- Construct load-bearing anchor systems to protect rock climbing routes
- Employ facilitation strategies to place participants at the intersection of exploration and experimentation

University Park, PA

August 2018 - Present

Relevant Coursework

Dynamics/Controls Aerospace Autonomy, Nonlinear & Linear Control Theory, Orbit and Attitude Control of Spacecraft
Aerodynamics/Structures Structural Dynamics, Aerodynamics, Propulsion, Aeronautics, Statics, Strength of Materials
Mathematics/Analysis Differential Equations, Multivariable Calculus, Linear Algebra, Aerospace Analysis

Relevant Skills

Software Development MATLAB/Simulink - Proficient, C/C++ - Intermediate, Python - Beginner, LaTeX - Proficient, Git - Proficient
Embedded Systems Linux - Intermediate, Raspberry Pi - Intermediate, Arduino - Intermediate
Design/Fabrication SolidWorks - Intermediate, AutoCAD - Intermediate, Machining - Beginner

Honors & Awards

2020 **First Place**, Penn State Undergraduate Research Exhibition, Engineering Category *University Park, PA*
2020 **Scholar**, NASA Pennsylvania Space Grant Consortium *University Park, PA*
2018 **Awardee**, The President's Freshman Award *University Park, PA*
2017 **Scholar**, Schreyer Academic Excellence *University Park, PA*

Presentations

Penn State Undergraduate Research Exhibition *University Park, PA*
<OPTIMAL DEXTERITY FOR TENSEGRITY ROBOTIC ARM> *Apr. 2020*
• Introduced concepts and initial prototyping of a novel tensegrity robotic arm
• Awarded **First Place** in the Engineering Category